LARGE EDDY SIMULATION OF THE FLOW AROUND BLUFF BODY WITH DRAG REDUCTION DEVICE

BY

KHALID QAIED AL-ANAZI

A Thesis Presented to the

DEANSHIP OF GRADUATE STUDIES

KING FAHD UNIVERSITY OF PETROLEUM & MINERALS

DHAHRAN, SAUDI ARABIA

In Partial Fulfillment of the
Requirements for the Degree of

MASTER OF SCIENCE

In

AEROSPACE ENGINEERING

MARCH 2010 (G)

KING FAHD UNIVERSITY OF PETROLEUM & MINERALS
DHAHRAN 31261, SAUDI ARABIA

DEANSHIP OF GRADUATE STUDIES

This thesis, written by Khalid Q. AL Anazi under the direction of his thesis advisor and approved by his thesis committee, has been presented to and accepted by Dean of Graduate Studies, in partial fulfillment of the requirements for the degree of MASTER OF SCIENCE IN **AEROSPACE ENGINEERING.**

Thesis Committee

Dr. Abdullah M. Al-Garni (Advisor)

Dr. Ahmed Z. Al-Garni (Member)

Dr. Ayman H. Kassem (Member)

Dr. Ahmet Z. Sahen (Member)

Dr. Maged A.I. El-Shaarawi (Member)

Dr. Ahmed Z. Al-Garni
(Department Chairman)

Dr. Salam A. Summo
(Dean of Graduate Studies)

19/6/10
Date

Dedicated to

My Loving Parents

ACKNOWLEDGMENT

In the name of ALLAH, the Most Beneficent, the Most Merciful.

All praise and glory be to ALLAH (SWT) who gave me the courage and patience to carry out this work and peace and blessings of ALLAH be upon the prophet, Mohammad (SAWA). Acknowledgment is due to King Fahd University of Petroleum & Minerals for supporting this research and my master program.

I wish to express my appreciation to my thesis advisor Dr. Abdullah M. AL Garni for his invaluable support, encouragement, patience and guidance. I wish also to thank my thesis committee members Dr. Ahmed Z. AL Garni , Dr. Ayman Kassem, and Dr. Maged A.I. El-Shaarawi and Dr. Ahmet Sahen for their valuable comments and suggestion. Completion of this work would not be possible without their support. I would also like to thank the chairman of the Aerospace Engineering Department Dr. Ahmed Z. AL Garni and all the AE department faculty members and staff for their support.

Finally, a great thank to my parents for their pray, help and support. Also I would like to thank all my friends and family members for their encouragement and support.

TABLE OF CONTENTS

LIST OF FIGURES

LIST OF TABLES

THESIS ABSTRACT

NAME: KHALID QAIED K. AL ANAZI

TITLE: LARGE EDDY SIMULATION OF THE FLOW AROUND BLUFF BODY WITH DRAG REDUCTION DEVICE

MAJOR FIELD: AEROSPACE ENGINEERING

DATE OF DEGREE: March 2010

This thesis focuses on the use of LES to simulate the flow around elliptical bluff body with blunt trailing edge fitted with open base cavity. The main objective of this study is to determine the effects of the cavity on the drag of the body. A secondary but important objective is to demonstrate that LES can provide accurate representation of the flow around this bluff body. Moreover, LES results can complement the available experimental results in order to provide a much better understanding of the flow. The simulations were carried out at a Reynolds number of 2.6×10^4 based on the height of the body using Spalart-Allmaras RANS model while the LES were performed using Smagorinsky dynamic model. A grid-independence test was conducted using three grids which contain 0.85M, 1.3M and 1.7M cells, respectively. This test shows that the results are grid-independent. The LES results predicted the mean flow field in the near wake with good accuracy as compared to the experimental mean flow field obtained. The base pressure results show that the base pressure

coefficient for the base model was around -0.56, which agrees well with the experimental results .By attaching the cavity, the base pressure has increased. The increase in base pressure coefficient was around 44% using 1/3 h cavity and this agrees well with the experimental measurements. The RANS predicted drag coefficient of 0.56 for the base model and 0.471 for the cavity model. This represents a difference of 8% for the base model and 34% for the cavity model when compared with experiment drag coefficients (0.61 for the base model and 0.35 for the cavity model). For the LES, the drag coefficient of the base model was around 0.65 (6.5% difference) and using the cavity, the drag coefficient was reduced to around 0.37 (5.74% difference).

Details of the mean velocity components have been compared with experimental data at various locations in the wake region of the flow. Observation on the comparison between LES and RANS shows that LES predicted the mean flow field more accurately than RANS particularly downstream the recirculation regions. The length of the recirculation region was over predicted by RANS compared to LES. The prediction of this length by LES was in excellent agreement with experimental measurement.

MASTER OF SCIENCE DEGREE

KING FAHD UNIVERSITY OF PETROLEUM & MINERALS

Dhahran, Saudi Arabia

THESIS ABSTRACT (Arabic)

ملخص البحث

درجة الماجستير في العلوم الهندسية

الاسم : خالد بن قعيد العنزي

عنوان الرسالة : المعامل الحسابي LES حول جسم مبسط مع جهاز لتقليل المقاومة

التخصص : هندسة الطيران والفضاء

تاريخ التخرج : آذار 2010

هذه الأطروحة تركز على استخدام النموذج الحسابي (LES) لحساب الهواء المضطرب حول جسم بيضاوي الشكل وآخر مماثل له مع إلصاق تجويفه هوائية مفتوحة في نهايته . الهدف الأساسي من هذه الدراسة هو تحديد تأثير إضافة التجويفة الهوائية المفتوحة لهذا الجسم. أما الهدف الأخر والمهم أيضا هو توضيح أن النموذج الحسابي (LES) قادر على إظهار نتائج حسابيه دقيقه حول هذا الجسم إضافة إلى إثبات أن النموذج الحسابي (LES) يستطيع أن يكمل حسابات التجربة العملية ليقدم نتائج أعمق وأدق للهواء المضطرب حول مثل هذه الأجسام . الحسابات كانت عند معامل رينولدز 26000 اعتمادا على ارتفاع الجسم(h) باستخدام النموذج الحسابي سبالارت ألماراس (Spalart-Allmara) من النموذج RANS والنموذج الحسابي سماقرنسكي_الديناميكي (Smagorinsky dynamic model) من النموذج (LES) . لقد تم عمل ثلاث شبكات حسابيه تحتوي على 0.85 و 1.3 و 1.7 مليون خليه للتأكد من أن النتائج ا لحسابية لا تعتمد على حجم الشبكة, وقد أظهرت هذه النتائج عدم اعتماد النتائج على أي من هذه الشبكات . كما أن نتائج السرعة المتوسطة للمعامل الحسابي (LES) كانت قريبه جدا من نتائج السرعة المتوسطة التي أجريت في التجربة العملية حيث أن نتائج الضغط الأساسي أظهرت أن معامل الضغط الأساسي للجسم من دون إضافة التجويفة الهوائية حوالي - 0.56 والتي كانت قريبه جدا من نتائج التجربة العملية أما بإضافة التجويفة الهوائية المفتوحة (1/3h) فقد ارتفع الضغط الأساسي حيث كان مقدار الزيادة حوالي 44% والتي تتفق تماما مع التجربة العملية. أما باستخدام النموذج الحسابي (RANS) فكان معامل المقاومة الهوائية حوالي 0.56 للجسم بدون تجويفه و 0.471 بعد إضافة التجويفة إليه والذي يمثل اختلاف حوالي 8% عن الجسم الأساسي و 34%عن نفس ا لجسم بعد إضافة التجويفة إليه وذلك عند مقارنة النتائج مع التج ربة العملية (0.61 للجسم

الأساسي و 0.35 للجسم بعد إضافة التجويفة إليه). أما بالنسبة للنموذج الحسابي (LES) فكان معامل مقاومة الهواء حوالي 0.65 (6.5% فارق عن التجربة) بالنسبة للجسم الأساسي و بعد إضافة التجويفة إليه فقد انخفض حوالي 0.37 (5.74% فارق عن التجربة).

تفاصيل النتائج الحسابية للسرعة المتوسطة تم مقارنتها مع التجربة العملية مركزا على الجانب الخلفي للجسم و تم ملاحظة الفرق بين الطريقتين الحسابيتين (LES) و(RANS) حيث أثبتت الطريقة الحسابية (LES) أنها أدق من الطريقة الحسابية (RANS) خاصة في الجانب الخلفي للجسم حيث تتكون الدوامات الهوائية, وذلك أن طول الدوامة الهوائية كانت غير دقيقه باستخدام طريقة (RANS) أما باستخدام طريقة (LES) فكانت دقيقه جدا مقارنة بالتجربة العملية.

درجة شهادة الماجستير

جامعة الملك فهد للبترول و المعادن

الظهران, المملكة العربية السعودية

NOMENCLATURE

A	Projected area in the flow direction (m^2)
C_{dym}	Dynamic parameter of Smagorinsky constant
C_D	Drag Coefficient; $C_d = \frac{D}{0.5\rho U^2 A}$
C_L	Lift coefficient; $C_L = \frac{L_f}{0.5\rho U^2 A}$
C_P	Pressure coefficient; $C_P = \frac{P - P_\infty}{0.5\rho U^2}$
C_s	Smagorinsky constant
CFD	Computational Fluid Dynamics
DES	Detached Eddy Simulation
D	Drag force; (N)
DNS	Direct Numerical Simulation
F	Pressure force; (N)
f_s	Shedding frequency of vortices; (Hz)
H	Body height; (m)
G_v	Production of turbulent viscosity
L	Body Length; (m)
L_f	Lift force; (N)
LES	Large Eddy Simulation

N-S	Navier- Stokes
P	Pressure; (N/m^2)
P_∞	Freestream Pressure; (N/m^2)
q_{SGS}	Velocity scale; (N/m)
RMS	Root Mean Square
Re	Reynolds number; $\mathrm{Re} = \frac{VL}{\nu}$
SGS	Subgrid Scale
$\bar{S}$	Strain rate tensor; (1/s)
S	Second (time unit)
St	Strouhal Number; $St = \frac{f_s}{u} h$
$S_{\tilde{\nu}}$	User-defined source term.
T	Time scale; (s)
τ_{ij}	Reynolds stress; (N/m^2)
U	Streamwise velocity; (m/s)
u	Fluid velocity; (m/s)
$\bar{u}$	Filtered resolved velocity; (m/s)
u'	Filtered unresolved velocity; (m/s)
u^*	Frictional velocity (m/s), $u^* = \sqrt{\frac{\tau}{\rho}}$; (m/s)
X	Dimension along x-axis; (m)

Y	Dimension along y-axis; (m)
Y	Wall-normal distance; (m)
Y_v	Destruction of turbulent viscosity occurs in the near-wall region
y^+	Non-dimensional distance from the wall; $y^+ = \frac{yu^*}{\nu}$
Z	Dimension along z-axis; (m)
Δt	Time step; (s)
Δx , Δy, Δz	Streamwise, Crossstream and Spanwise grids spacing; (m)

Greek

Δ	Length scale; (m)
ρ	Density; (kg/m^3)
N	Kinematic viscosity of the flow; (m²/s)
ν_{SGS}	SGS eddy viscosity; (m^2/s)
ν_τ	Eddy viscosity; (m^2/s)
μ_τ	Turbulent viscosity; (m²/s)

CHAPTER 1

INTRODUCTION

The flow around bluff bodies is complex, highly three-dimensional and unsteady. The experimental tools used to obtain flow field provide limited information about the flow e.g. mean flow field. Recent decades have seen increasing use of numerical methods to solve the Navier-Stokes Equations around complex bodies. This has become feasible both by the availability of ever-improving fast computers and by the development of computational fluid dynamics. The most straightforward way to simulate a fluid flow is direct numerical simulation (DNS), so designated because no turbulence model is required. The feasibility of DNS is limited to low-Reynolds-number flows, because the number of mesh points for a DNS is proportional to $Re^{9/4}$ (Launder and Spalding [1]),which makes it impossible for current or near-future computers to simulate high-Reynolds-number flows. To overcome this difficulty, researchers have developed different methods of treating turbulence effect. Most of these methods fall into two categories, namely Reynolds-averaged Navier-Stokes (RANS) equations and large eddy simulation (LES). Compared with the LES method, the RANS method has a longer history of application, and a lower computational cost. Much experience has been accumulated with this method, especially with the k-ε version of the method. Despite its achievements, RANS is not sufficiently accurate for separating and reattaching flows. In addition, steady RANS provide only limited information about the flow field since it solves the time- averaged Navier-Stokes Equations. For high Reynolds number wall bounded flows, the computational cost increases dramatically because of the very large

number of cells required in the boundary layer and is comparable to Direct Numerical Simulation (DNS). Hence some kind of wall-model is necessary to model the effect of solid wall. The LES uses spatial averaging and only simulates large-scale motions explicitly, while leaving small-scale eddies for modeling. Such an approach to reproduce the turbulence effect is based on two experimental observations (Launder and Spalding [1]; Arpaci and Larsen [2]). One is that large-scale eddies in a turbulent flow which depend on the configuration of the flow, are anisotropic, and contain most of the energy. The other observation is that small-scale eddies in turbulent flows which are more independent of the flow, are isotropic, and contain a small part of the total energy. These observations suggest the possibility of modeling the small-scale eddies while explicitly computing the large-scale flow. So, in this study, large eddy simulation (LES) will be used to compute the flow around elliptical bluff body fitted with base cavity to determine its drag effects.

1.1 Literature Review

Control of bluff body flows both from the point of view of drag reduction as well as suppressing unsteady forces caused by vortex shedding has been an area of considerable interest in engineering applications. The basic aim in the different control methods involves direct or indirect manipulation of the near-wake structure leading to weakening or suppressing of vortex shedding.

Zdravkovich [3] used various devises using the passive control techniques in the context of a two-dimensional circular cylinder that can be broadly classified under surface protrusions (e.g., strakes, fins and wires), shrouds (e.g., perforation, gauze and slats) and

near-wake stabilizer (e.g., splitter plates and base bleed). Nash [4], Tanner [5] and Viswanath [6] used another technique involving base modifications such as cavities with and without ventilation. All the techniques have been used by the researchers show an effect on the drag reduction and base pressure changes. Maxworthy[7] introduced a solid cylinder with axis along the freestream direction (like a cylindrical sting) in the wake of a sphere to obtain an effect similar to that of a splitter plate behind circular cylinder, but found that there was no significant change in the base pressure.

Quadflieg [8] found that a thin wire placed close to the location of the turbulent separation line forced the unsteady separation to become steady, which reduced the drag of a sphere in the supercritical range by nearly 50%. Petrusma and Gai [9] used the method where they explored the possibility of drag reduction using a segmented trailing edge for both laminar and turbulent separating boundary layers and determined the optimal geometry of the rectangular segment. Tombazis and Bearman [10] used in-homogonous method to reduce the drag. They installed a wavy trailing edge on a blunt-based bluff body and found that the waviness of the trailing edge produces vortex dislocation in the wake and thus the base pressure got increased.

Park et al. [11] further simplified the work of active forcing into a passive device, done by Kim et al. [12], by developing a new passive device which is a small tab, mounted on part of the trailing edge of a bluff body, for effectively attenuating the vortex shedding and reducing drag. It is shown that that the tab effectively disturbs the wake such that the two-dimensional wake structure turns into a three-dimensional one.

Bearman [13] examined the flow in the wake of a two-dimensional model with a blunt trailing edge. The ratio of total boundary layer thickness at the trailing edge to model base height was approximately 0.5. Measurements were taken of base pressure and vortex shedding frequency together with traverses of the wake. Measurements along the wake showed a peak in the RMS velocity-fluctuation at a distance equal to one base height from the model rear face which is called the fully formed vortex position. A model fitted with splitter plates was also investigated. For each plate tested, a position of the fully formed vortex was found, and its distance from the model base was discovered to be inversely proportional to the base pressure coefficient.

Michael and Craig [14] used PIV system which has been used to study the near-wake structure of a two-dimensional base in subsonic flow to determine the fluid dynamic mechanisms of observed base drag reduction in the presence of a base cavity. Experiments were done over a range of free stream Mach numbers up to 0.8, including local flow field velocities over 300 m/s. Effects of the base cavity on the von Karman vortex street wake were found to be related to the expansion and diffusion of vortices near the cavity. The base cavity effects are also less significant at higher free stream velocities due to the formation of vortices further downstream from the base. The base cavity drag reduction was found to be mainly due to the displacement of the base surface to a location upstream of the low-pressure wake vortices, with only a slight modification in the vortex street itself.

Bahram et al. [15] conducted an experimental and computational investigation of a drag reduction device for 3-D bluff bodies. Unsteady base pressure, hot-wire velocity fluctuations and Particle Image Velocimetry (PIV) measurements of the near wake of the models

(baseline and the modified models) are reported. He found that, the drag reduction device suppresses large-scale turbulent motions in the wake. Also, the results showed a reduction of the turbulence intensity with the device in place. The effect of the drag reduction device on the length of the recirculation region in the near wake was small. Krajnovic and Davidson [16] performed LES on 25° rear slant angel Ahmed model at a Reynold number of Re = 2×10^5. The results were compared with experimental one at higher Reynolds number (Re = 7.68×10^5). The LES results indicated that for the existing geometry the external vehicle flows at high Reynolds number becomes insensitive to Reynolds number. It was found that the geometry rather than the viscosity dictates the character of the flow and the positions of flow separations. Also it was observed that while using lower Reynolds number the near wall energy carrying coherent structures can be resolved and the flow could be predicted more accurately. This observation raised hope that flow around real cars could be simulated with LES at reduced Reynolds numbers.

Hinterberger et.al [17] conducted experiments on 25° rear slant angle Ahmed models and concluded that the results obtained through Large Eddy Simulation (LES) are promising. The comparisons with the experiments showed well captured flow structures. Sohankar et al. [18] employed LES on the simulation of a series of flows around a square cylinder ranging from Reynolds number of a few hundreds to 2.2×10^4. Simulated results concluded that the Strouhal number was close to other experimental findings of slightly higher Reynolds number but the flow profiles differ significantly between the two-dimensional and the three-dimensional flow. A longer recirculation length has been predicted by the two dimensional simulation. Closer agreement of the mean drag and pressure coefficients with experimental

result has been observed from the three-dimensional calculation. Their results are in good agreement with Okajima [19] who pointed out that flow at these Reynolds numbers shows strong three-dimensional characteristics. He also pointed out that increasing the spanwise length (the depth of the cylinder) has a rather small influence on the mean flow parameters at low Reynolds number.

Yu and Kareem [20] applied LES with the Smagorinsky sub-grid model to the flow around rectangular sections to observe the changes of separated type of flow to reattached flow as the aspect ratio increases. From the changes of the pressure profiles along the side surface of the cylinders, reattachment of flow has been reported, in agreement with the experimental observations. Compared to the earlier two-dimensional LES of Yu and Kareem on the flow around rectangular sections, the results showed discrepancies especially in the prediction of the Strouhal number. Ferziger [21] was among the pioneers in doing the LES of flow over a surface mounted cube at Reynolds number 4×10^4, with good correspondence to compare with experiment. This geometry was investigated recently by Krajnovic and Davidson [16], at Reynolds number 4×10^4 with different LES models. Their results showed that the LES models are capable of predicting this flow field with acceptable accuracy even for coarse grid.

1.2 Present Investigation

This work is a part of a combined experimental and numerical investigation conducted at the Department of Aerospace Engineering, KFUPM to study the effects of various base cavities on the aerodynamics of elliptical bluff body. The experimental part is being conducted by my colleague Aravind ChandraMohan (AbduRahman), a research assistant at the AE Department. In the experimental work, various shapes and lengths of cavity were tested to determine their effects on steady and unsteady base pressures and aerodynamic drag as well as wake structure behind the cavity. The numerical part will focus on using CFD techniques to determine the effects of base cavities on the flow around the reference geometry. Since the CFD results have to be validated against experimental data collected through the wind tunnel tests, it is decided to conduct the numerical investigation at the experimental Reynolds number ($Re = 2.7\times10^4$). It is important to mention that due to the limited computational resources available at the department and the university, this study will compute the flow around the reference geometry and the best drag reduction cavity (1/3 h open base cavity). This cavity is selected based on the experimental results. The LES requires massive computing resources and it is hoped that these resources will be available in the near future.

1.3 Objectives of the Study

The study focuses on the use of LES to simulate the flow around elliptical bluff body with blunt trailing edge fitted with open base cavity. The main objective of this study is to determine the effects of the cavity on the drag of the body. A secondary but important objective is to demonstrate that LES can provide accurate representation of the flow around this bluff body. Moreover, LES results can complement the available experimental results in order to provide a much better understanding of the flow around this body

CHAPTER 2

MATHEMATICAL FORMULATION

2.1 Equations of Flow

The equation that govern the motion of viscous fluid has been known for more than a century. These equations are known as continuity (conservation of mass) , momentum (conservation of momentum) and energy (conservation of energy) and used to solve for the primary unknowns which include the pressure, P, components of velocity vector u,v,w and temperature, T. For isothermal flows , the energy equations is not solved and the equations are reduced to conservations of mass and momentum.

$$\frac{\partial u_i}{\partial x_i} = 0 \quad \text{..... (2.1)}$$

$$\frac{\partial u_i}{\partial t} + u_j \frac{\partial u_i}{\partial x_j} = -\frac{1}{\rho}\frac{\partial P}{\partial x_i} + \frac{\partial}{\partial x_j}\left[\nu \frac{\partial u_i}{\partial x_j}\right] \quad \text{.....(2.2)}$$

By solving these equations, the pressure and velocity field can be obtained throughout the flow. In turbulence flows, these equations are impossible to solve with current mathematical techniques. However , they can be modeled on a digital computer using finite differences , elements or volumes. The next section discusses turbulence modeling.

2.2 Turbulence Models

Turbulent flow is highly unsteady and irregular. Generally, simulations of flow can be done by filtering or averaging the Navier-Stokes equations. The latter are usually referred as the Reynolds Averaged Navier Stokes (RANS) models, where the unsteadiness of the flow is averaged out. In the RANS model, all aspects of turbulence are modeled. On the contrary, the space filtering method resolves a major portion of the turbulent scales numerically and models only the small scales eddies, enabling the dynamic features of the flow to be captured. In all CFD simulations, a mesh independence test is important in order to achieve a statistically accurate and converged solution. This means that changing the mesh size will not significantly affect the numerical solutions. A mesh independence test is usually done by refining the mesh resolution of the simulations gradually to achieve a constant solution.

2.3 Reynolds Averaged Navier –Stokes Modeling (RANS Modeling)

Flow is separated into mean and fluctuating components in the RANS approach to turbulence,

$$u = \overline{U} + u' \quad \text{..... (2.3)}$$

Physically, the time averaging velocity component is defined as,

$$\bar{u} = \frac{1}{T}\int_0^T u\,dt \quad \text{.....(2.4)}$$

where T is the averaging time of the simulation, usually chosen to be large compared to the typical timescale of turbulent fluctuation.

Substituting equation 2.3 into the Navier-Stokes equations for time averaging, one obtains the time averaged Navier-Stokes equations,

$$\frac{\partial \overline{u_i}}{\partial t} + \overline{u_j}\frac{\overline{u_i}}{\partial x_j} = -\frac{1}{\rho}\frac{\partial \overline{p}}{\partial x_i} + \frac{\partial}{\partial x_j}\left[\nu \frac{\partial \overline{u_i}}{\partial x_j} - \overline{u_i u_j}\right] \quad \text{.....(2.5)}$$

where ρ, P and ν represent the air density, pressure and kinematic viscosity of the flow respectively.

The statistical averaging of the Navier-Stokes equations give rises to the unknown term $\overline{u_i u_j}$, which are the correlation between the fluctuating velocity components and is known as the Reynolds Stress term. The existence of the Reynolds stress means there is no longer a closed set of equations, and turbulence model assumptions are needed to estimate the unknowns to solve this closure problem.

2.3.1 Spalart-Allmaras Model

The Spalart-Allmaras model is a one-equation model that solves a modeled transport equation for the kinematic eddy (turbulent) viscosity. It has been shown to give good results for boundary layers subjected to adverse pressure gradients. In FLUENT, the near-wall gradients of the transported variable in the model are much smaller than the gradients of the transported variables in other models.

The transported variable in the Spalart-Allmaras model, $\tilde{\nu}$, is identical to the turbulent kinematic viscosity except in the near-wall (viscous-affected) region. The transport equation for $\tilde{\nu}$ is:

$$\left(\rho\nu\right)+\frac{\partial}{\partial x_i}\left(\rho\nu u_i\right)=G_\nu+\frac{1}{\sigma\nu}\left[\frac{\partial}{\partial x_j}\left\{\left(\mu+\rho\nu\right)\frac{\partial\nu}{\partial x_j}\right\}+C_{b2}\rho\left(\frac{\partial\nu}{\partial x_j}\right)^2\right]-Y_\nu+S_\nu \quad \text{.....(2.6)}$$

The turbulent viscosity, μ_t , is computed from

$$\mu_t=\rho\bar{\nu}f_{v1} \quad \text{.....(2.7)}$$

where the viscous damping function, f_{v1}, is given by

$$f_{v1}=\frac{x^3}{x^3+C_{v1}^3} \quad \text{.....(2.8)}$$

and

$$x\equiv\frac{\bar{\nu}}{\nu} \quad \text{.....(2.9)}$$

So, the production term, C_ν, is modeled as

$$C_\nu=C_{b1}\rho\bar{S}\bar{\nu} \quad \text{..... (2.10)}$$

Where

$$\bar{S}\equiv S+\frac{\bar{\nu}}{\kappa^2 d^2}f_{v2} \quad \text{.....(2.11)}$$

and

$$f_{v2}=1-\frac{x}{1+xf_{v1}} \quad \text{.....(2.12)}$$

C_{b1} and κ are constants, d is the distance from the wall, and S is a scalar measure of the deformation tensor which is based on the magnitude of the vorticity:

$$S \equiv \sqrt{2\Omega_{ij}\Omega_{ij}} \quad \text{.....(2.13)}$$

where Ω_{ij} is the mean rate-of-rotation tensor and is defined by

$$\Omega_{ij} = \frac{1}{2}\left(\frac{\partial u_i}{\partial x_j} - \frac{\partial u_j}{\partial x_i}\right) \quad \text{..... (2.14)}$$

The justification for the default expression for S is that, in the wall-bounded flows that were of most interest when the model was formulated, the turbulence production found only where vorticity is generated near walls. However, it has since been acknowledged that one should also take into account the effect of mean strain on the turbulence production, and a modification to the model has been proposed and incorporated into FLUENT. This modification combines the measures of both vorticity and the strain tensors in the definition of S:

$$S \equiv \left|\Omega_{ij}\right| + C_{prod} \min\left(0, |S_{ij}| - \left|\Omega_{ij}\right|\right) \quad \text{.....(2.15)}$$

Where

$$C_{prod}=2.0,\ \left|\Omega_{ij}\right| \equiv \sqrt{2\Omega_{ij}\Omega_{ij}},\ |S_{ij}| \equiv \sqrt{2S_{ij}S_{ij}} \quad \text{.....(2.16)}$$

with the mean strain rate, S_{ij}, defined as

$$S_{ij} = \frac{1}{2}\left(\frac{\partial u_j}{\partial x_i} + \frac{\partial u_i}{\partial x_j}\right) \quad \text{.....(2.17)}$$

The destruction term is modeled as

$$Y_\nu = C_{w1}\rho f_w \left(\frac{\bar{\nu}}{d}\right)^2 \quad \text{.....(2.18)}$$

Where

$$f_w = g\left[\frac{1+C_{w3}^6}{g^6+C_{w3}^6}\right]^{1/6} \quad \text{.....(2.19)}$$

Where

$$g = r + C_{w2}\left(r^6 - r\right) \quad \text{.....(2.20)}$$

And

$$r \equiv \frac{\bar{\nu}}{\bar{S}\kappa^2 d^2} \quad \text{.....(2.21)}$$

C_{w1}, C_{w2} and C_{w3} are constants, and $\bar{S}$ is given by equation (2.11). Note that the modification described above to include the effects of mean strain on S will also affect the value of $\bar{S}$ used to compute r.

The model constants C_{b1}, C_{b2}, $\sigma_{\bar{\nu}}$, $C_{\nu 1}$, C_{w1}, C_{w2}, C_{w3} and κ have the following default values:

$$C_{b1} = 0.1355, \quad C_{b1} = 0.622, \quad \sigma_{\bar{\nu}} = \frac{2}{3}, \quad C_{\nu 1} = 7.1, \quad C_{w1} = \frac{C_{b1}}{\kappa^2} + \frac{\left(1+C_{b2}\right)}{\sigma_{\bar{\nu}}}, \quad C_{w2} = 0.3,$$

$$C_{w3} = 2, \kappa = 0.4187$$

2.4 Large Eddy Simulation (LES)

Large eddy simulation (LES) is classified as a space filtering method in CFD. LES directly computes the large-scale turbulent structures which are responsible for the transfer of energy and momentum in a flow while modeling the smaller scale of dissipative and more isotropic structures. In order to distinguish between the large scales and small scales, a filter function is used in LES. This filter function dictates which eddies are large by introducing a length scale, usually denoted as Δ in LES. All eddies larger than Δ are resolved directly, while those smaller than Δ are approximated.

2.4.1 Filtering of Navier-Stokes Equations

In LES, the flow velocity u is separated into a filtered, resolved part $\bar{u}$ and a sub-filter, unresolved part , u',

$$u = \bar{u} + u' \quad \text{.....(2.22)}$$

The filter discretizes the flow spatially. Applying the filter function to equation (2.7), we have,

$$\bar{u}(x) = \int G(x, x')u(x')dx' \quad \text{.....(2.23)}$$

As mentioned, the filter function dictates the large and small eddies in the flow. This is done by the localized function $G(x, x')$. This function determines the size of the small scales [6],

$$G = \begin{cases} \frac{1}{\Delta}, if \ |x - x'| \le \frac{\Delta}{2} \\ 0, otherwise \end{cases} \quad \text{.....(2.23)}$$

By imposing the filter function in the continuity and the Navier-Stokes equations, one obtains the filtered equations governing the fluid flow in LES,

$$\frac{\partial \overline{u_i}}{\partial x} = 0 \quad \text{.....(2.24)}$$

$$\frac{\partial \overline{u_i}}{\partial t} + \frac{\partial}{\partial x_j}\left(\overline{u_i}\,\overline{u_j}\right) = -\frac{1}{\rho}\frac{\partial \overline{p}}{\partial x_i} + \nu \frac{\partial^2 \overline{u_i}}{\partial x_i x_j} - \frac{\partial \tau_{ij}}{\partial x_j} \quad \text{.....(2.25)}$$

The over bar denotes the space filtered quantities. The *p* and *v* represent the pressure and kinematic viscosity of the flow respectively.

The shear stress, τ_{ij},

$$\tau_{ij} = \overline{u_i u_j} - \overline{u_i}\,\overline{u_j} \quad \text{.....(2.26)}$$

is the subgrid stress(SGS) and is modeled.

2.4.2 Smagorinsky Model

To approximate the subgrid scal SGS Reynolds stress τ_{ij}, a SGS model can be employed. The most commonly used SGS models in LES is the Smagorinsky model. Where the effects of turbulence are represented by the eddy viscosity based on the well known Boussinesq hypothesis [22]. The Boussinesq hypothesis relates the Reynolds stress to the velocity gradients and the turbulent viscosity of the flow [23, 24]. It is therefore assumed that the SGS Reynolds stress τ_{ij} is proportional to the modulus of the strain rate tensor of the resolve eddies,

$$\tau_{ij} - \frac{\delta_{ij}}{3}\tau_{kk} = 2\nu_T \cdot \overline{S}_{ij} \quad \text{.....(2.27)}$$

where ν_T is the eddy viscosity and $\bar{s}_{ij}$ is the strain rate tensor,

$$\bar{S}_{ij} = \frac{1}{2}\left(\frac{\partial \overline{u_i}}{\partial x_j} + \frac{\partial \overline{u_j}}{\partial x_i} \right) \quad \text{.....(2.28)}$$

The eddy viscosity ν_T needs to be approximated in order to solve equation (2.9). Based on dimensional analysis, the following relationship has been obtained [25],

$$\nu_{SGS} \infty \ell q_{SGS} \quad \text{.....(2.29)}$$

where l is the characteristic length scale of the unresolved motion and q_{SGS} is the velocity scale. The length scale is taken as the filter width $\Delta = (\Delta_x \Delta_y \Delta_z)^{1/3}$ where Δ_x, Δ_y and Δ_z are the grid spacing in the x, y and z direction respectively [9]. By relating the velocity scale of the unresolved motion q_{SGS} to the gradients of the filtered velocity based on an analogy of the mixing length model [26], the eddy viscosity is written as,

$$\nu_T = (C_s \Delta)^2 \left| \bar{S} \right| \quad \text{.....(2.30)}$$

Where $\left| \bar{S} \right| = (2\overline{S_{ij}}\,\overline{S_{ij}})^{\frac{1}{2}}$ and C_s is the Smagorinsky constant and depends on the type of flow. For isotropic turbulent flow, the C_s value is usually around 0.18 to 0.2.

Basically, the Smagorinsky SGS model simulates the energy transfer between the large and the subgrid-scale eddies. Energy is transferred from the large to the small scales but backscatter (reverse of cascade process) sometimes occurs where flow becomes highly anisotropic, usually near to the wall. To account for backscattering, the length scale of the flow can be modified using Van Driest damping,

$$\left(C_s\Delta\right)=C_s\Delta\left(1-e^{\frac{-y^+}{25}}\right)\text{.....(2.31)}$$

where y^+ is the dimensionless distance from the wall. The Van Driest damping accounts for the reduced growth of the small scales near the wall which gives a smaller value of SGS viscosity in order to represent the flow more accurately.

The Smagorinksy model has been successfully applied to various flows as it is relatively stable and demands less computational resources among the SGS models. But some disadvantages of the model have been reported [23],

- Too dissipative in laminar regions.
- Requires special near wall treatment and laminar turbulent transition.
- C_s is not universal and depends on the type of flow
- Backscatter of flow is not properly modelled.

From Ferziger's [24] investigation, it has been pointed out that C_s is not constant in a flow and it is a function of the subgrid scale eddies and Reynolds number. The value of C_s varies between 10%-20% depends on the regimes of flow (wall bounded flow or transition flow) to achieve optimum flow prediction. Hence, the dynamic SGS model has been introduced.

This model employs a similar concept as the Smagorinsky model, with the Smagorinsky constant C_s replaced by the dynamic parameter C_{dym}. The parameter C_{dym} is computed locally as a function of time and space, which automatically eliminates the problem of using constant C_s. In the dynamic SGS model, another filter is introduced which takes into account the energy transfer in the dissipation range. Performing the double filtering

allows the subgrid coefficient to be calculated locally based on the energy drain in the smallest scales. For a more complete mathematical explanation of the dynamic SGS model, see Blazek [23].

Various researchers have employed both the dynamic and Smagorinksy SGS models in LES. Generally, the dynamic model predicted better agreement with experimental work in region of transition flow and the near wall region. Some advantages of the dynamic model over the Smagorinsky models are [23],

- Dynamic SGS automatically uses a smaller model parameter in isotropic flows.
- Near the wall, the model parameters need to be reduced; the dynamic SGS model adapts these parameters accordingly.
- Definition of length scale is always an issue in LES, the dynamic model compensates for the error in length scale by changing the value of the parame.

CHAPTER 3

NUMERICAL METHOD AND CFD

3.1 Geometry Details

The geometry of the bluff body with the relevant dimensions is shown in figure 3.1. The length of the body, L, is 290 mm and its height, h, is 50 mm. The forward part of the model has a length of 200 mm and is made of semi-elliptical profile with a semi-major axis to semi-minor axis ratio of 8:1. The rear part of the model has a length of 90 mm parallel-sided. Figure 3.2 shows the model fitted with open base cavity. The length of the cavity is 1/3 of the height, h. The cavity is displaced 3 mm from the upper and lower wall. The dimensions of this cavity were selected based on AbduRahman work [30] where he used similar cavities that used for drag reduction on full scale tractor and trailer for 3-d bluff body for other researchers. These cavities are expected to bring down the drag and experimented and investigated on the two-dimensional bluff body. Also the wake characteristics of flow is studied on attaching these cavities with the base model. The transition wires were attached at 20 % chord in both of models.

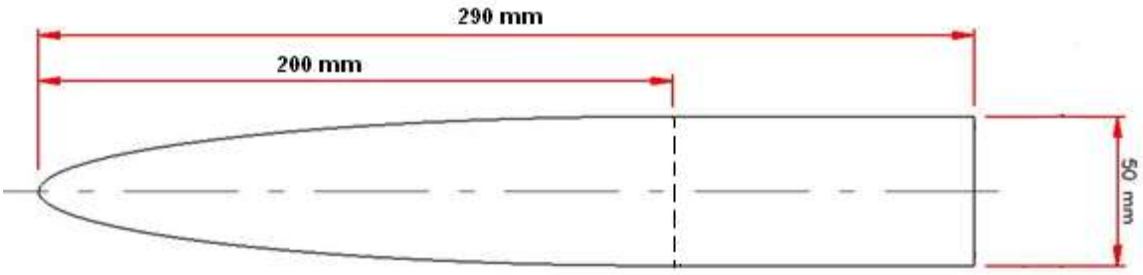

Figure 3.1 Schematic drawing of the base model with relevant dimensions.

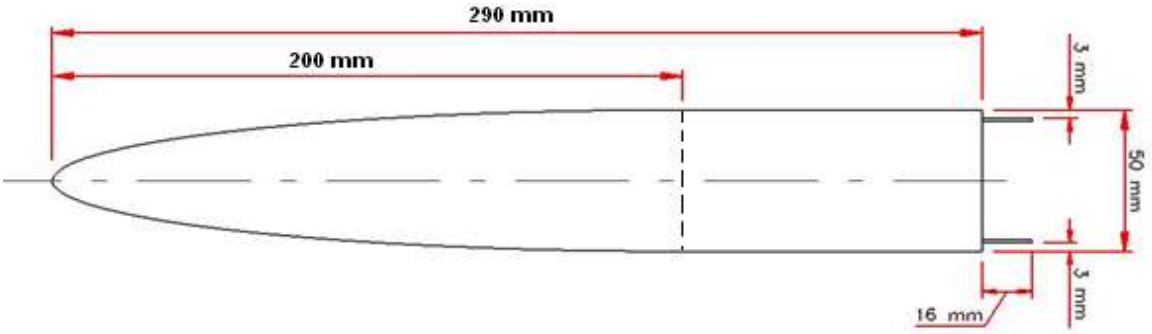

Figure 3.2 Schematic drawing of the base model fitted with open cavity(1/3h).

3.2 Numerical Method

3.2.1 Flow Solver

The computations were carried out using the segregated solver in FLUENT 6.3.26, a general-purpose CFD software. The numerical method is a cell-centered finite volume approach applicable to arbitrary cell topologies (e.g., hexahedral, tetrahedral). The gradient used to discretize the convection and diffusion terms in the flow conservation equation were computed using the cell-based Green-Gauss theorem. Diffusive fluxes are discretized using second-order accurate central differencing scheme. The convective fluxes were discretized using central differencing scheme. For the LES, an implicit, non-iterative fractional-step method (shown in figure 3.3) in combination with a second-order accurate scheme for time-discretezation was employed to advance the solution in time (Kim and Makarov [27]). The system of discretized governing equations are solved using a point-implicit, Gauss-Seidel relaxation along with an algebraic multi-grid method. The solver and the subgrid-scale turbulence model are fully parallelized.

In the segregated algorithm, the individual governing equations for the solution variables (e.g., u, v, w, p, T, k, etc.) are solved one after another . Each governing equation, while being solved, is “decoupled” or “segregated” from other equations as shown in Figure 3.3.. The segregated algorithm is memory-efficient, since the discretized equations need only be stored in the memory one at a time. However, the solution convergence is relatively slow, in as much as the equations are solved in a decoupled manner.

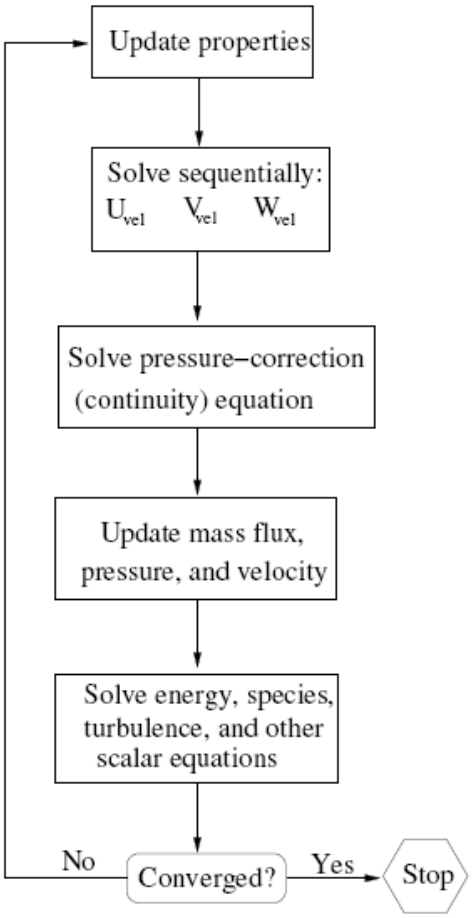

Figure 3.3 Overview of the segregated solution method.

For a transient simulation, all the equations are solved iteratively, for a given time-step, until the convergence criteria are met. Thus, advancing the solutions by one time-step requires a number of outer iterations as shown in figure 3.4(a). However, this requires significant computational efforts due to the large amount of outer iterations required for the solution to converge at each time step. The Non-Iterative Time Advancement (NITA) scheme proposed by Issa [31] provides an efficient alternative as shown in Figure 3.4(b). The idea behind this scheme is that the splitting error doesn't necessarily need to be zero but

rather the truncation error has to be the same order which reduce the outer iterations to a single outer iteration. Therefore, for LES computations, the equations were solved iteratively untile the solution becomes stable (~3000 time step) then the computation is shifted to NITA to speed up the transient simulation.

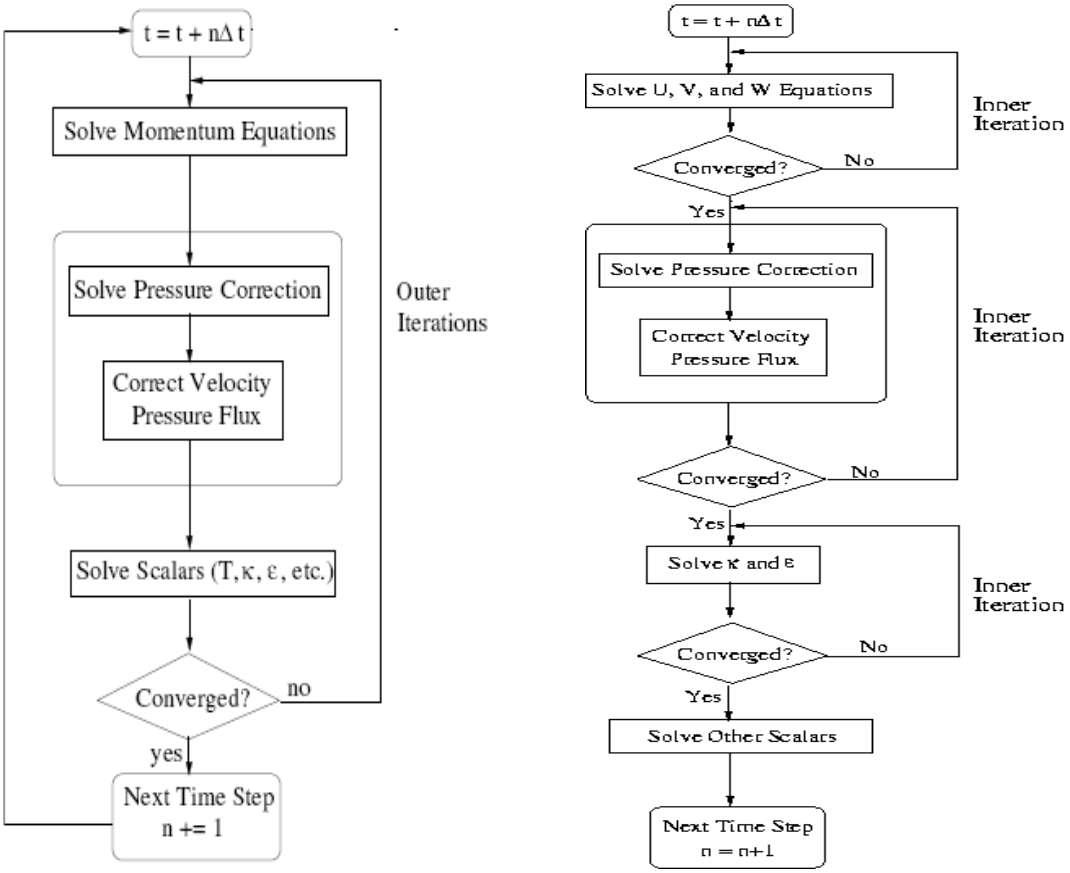

(a) (b)

Figure 3.3 Overview of the time advancement solution method: (a) iterative scheme and (b) non-iterative scheme.

3.2.2 Computational Domain

The grids were made using Gambit meshing code. In each grid, the size of the computational domain shown in figure 3.5 was kept the same and divided into four blocks for the base model and seven blocks for the base model with cavity (1/3 h) as shown in figures 3.6 and 3.7 respectively. The domain has a length of 31.5L in the streamwise direction, a height of 25L in the crossstream direction, and a depth of 0.7L in the spanwise direction. The leading edge of the body is located 11.5L from the inlet and the outlet is located 20L from the trailing of the body. At the inlet, a uniform velocity of 8 m/s is imposed, giving a Reynolds number of 2.6×10^4 based on the height of the model. At the outlet, a constant static (P=0) pressure is imposed. At the sides of the domain, a spanwise periodicity condition was applied (the flow at the spanwise boundaries are identical). On the model, the no-slip condition is used.

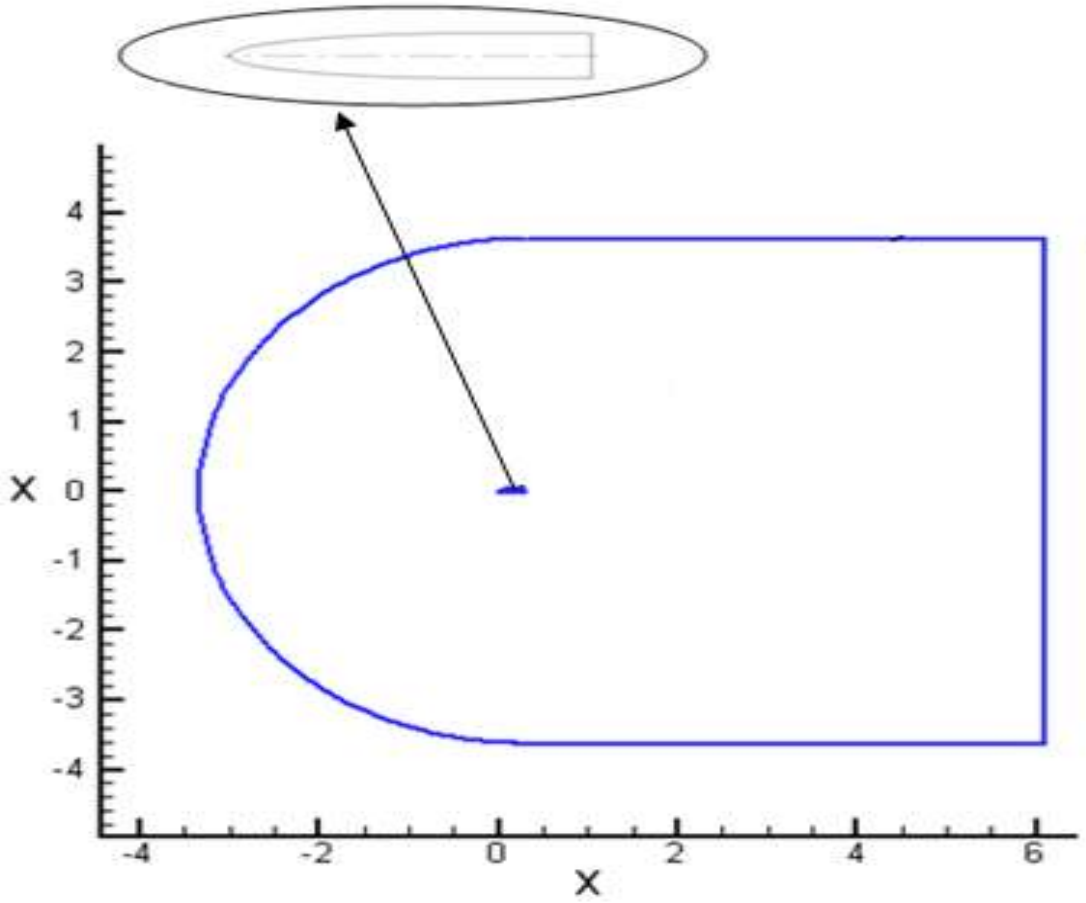

Figure 3.5 Computational domain used to simulate the flow around base and cavity model.

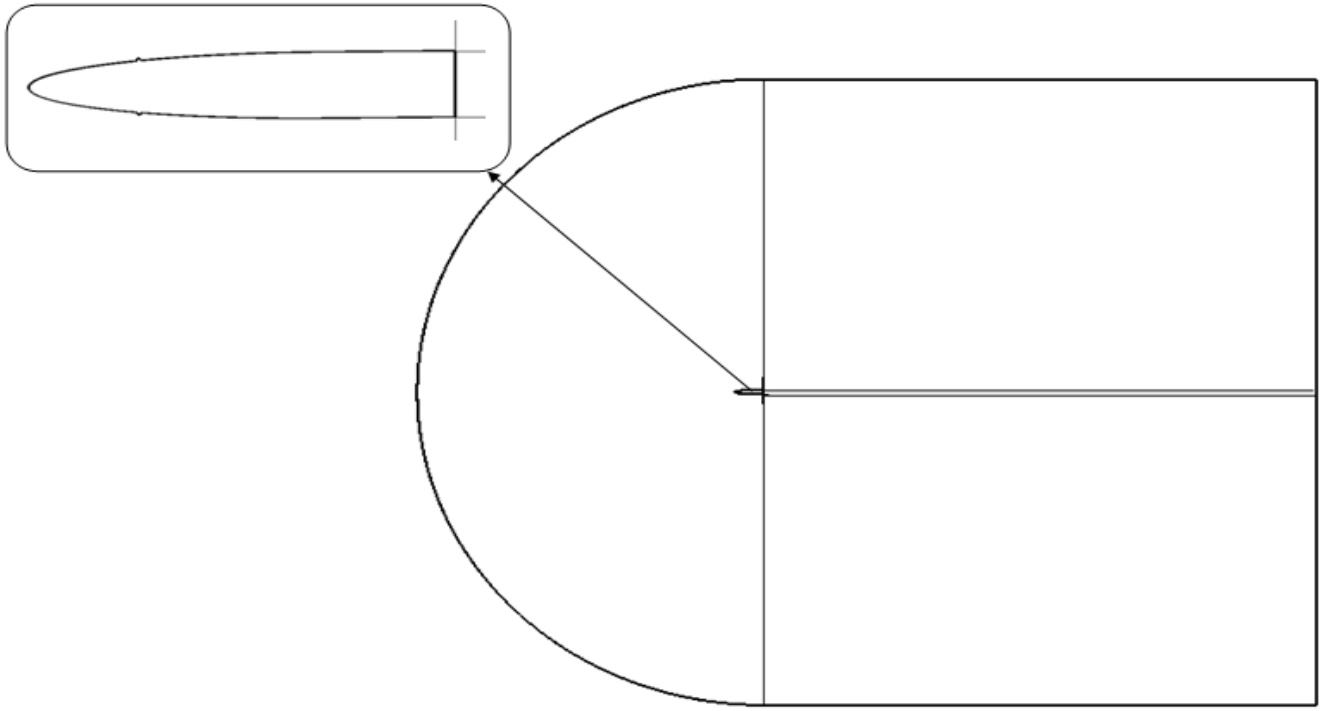

Figure 3.6 Computational domain for the base model divided into four blocks : whole domain and zoom view around the body.

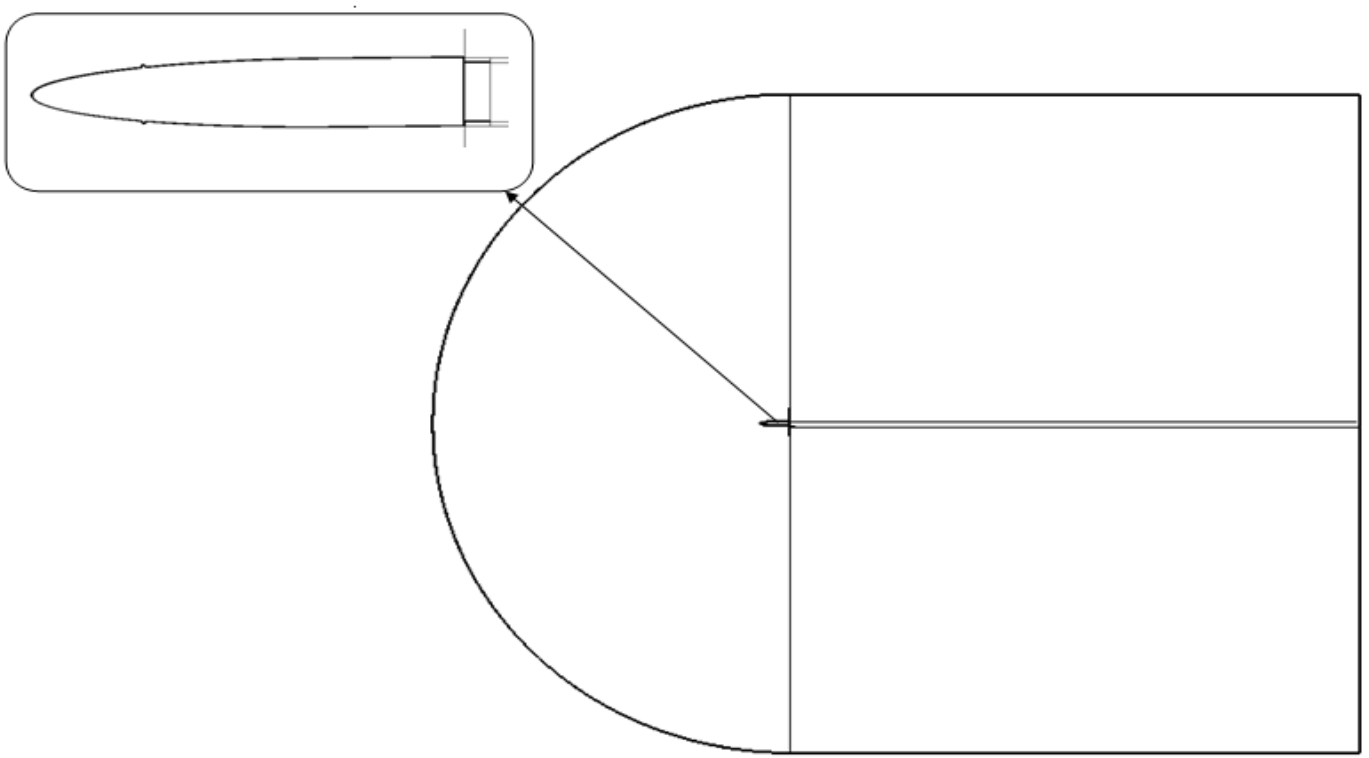

Figure 3.7 Computational domain divided into seven blocks for the base model with cavity (1/3 h): whole domain and zoom view around the body .

3.2.3 Computational Grids

Before carrying out LES computation, it was necessary to make sure that the solution is grid independent. In this regards, three C-H grids with different total number of cells were tested using RANS. The first grid, henceforth, G1, contains around 8×10^5 cells and the second grid,G2, contains around 1.3×10^6 cells. The third grid ,G3, contains around 1.7×10^6 cells. The computations were carried out using Spalart-Allmaras turbulence model. The streamwise and crossstream grids spacing, Δx and Δy, is increased linearly from the leading to the trailing edge. This results in Δx^+ and Δy^+ of 55.56 and 2.5 respectively and Δz^+ of 350 in the spanwise direction.

In RANS computation, it is common that the near wall situation is usually treated by introducing empirical formulas to represent the 'log law' region of the flow. This aims to avoid generating a very refined mesh in that region. In the wall function method, the viscosity sub-layer is represented mathematically by formulas to account for the effect of shear stress. For the LES technique, the mesh near the wall should be fine enough so that the boundary layer effects are taken into account. The refinement of the mesh in the boundary region is determined by the dimensionless parameter y^+.

$$y^+ = \frac{(yu^*)}{\nu} \quad \text{.....(3.1)}$$

where y is the wall-normal distance, u^* is the frictional velocity and ν is the molecular viscosity.

Physically, y^+ represents the normal distance of the grid points from the body wall. In LES, the y^+ value needs to be less than 3 to maintain mesh consistency and to represent the boundary layer correctly. The y^+ value around the surface of the current bluff bodies ranges between 1 and 1.5.

Figures 3.8 shows a sectional cut through the domain of the base model. It can be seen that more mesh is required near to the body to properly resolve the boundary layer. Moreover, more mesh in the weak region is required to capture the flow behavior in this region.

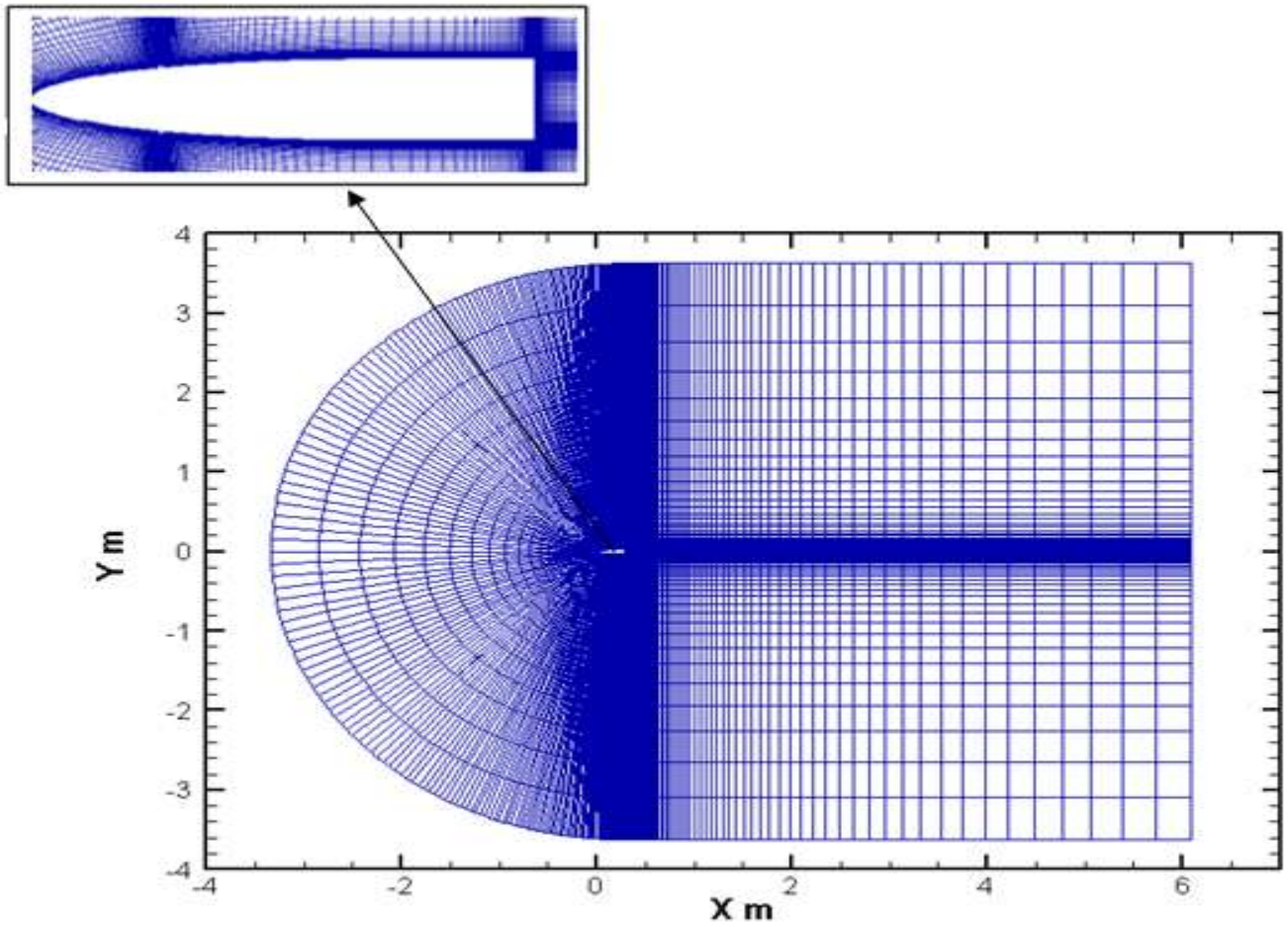

(a)

Figure 3.8 For caption see page 32.

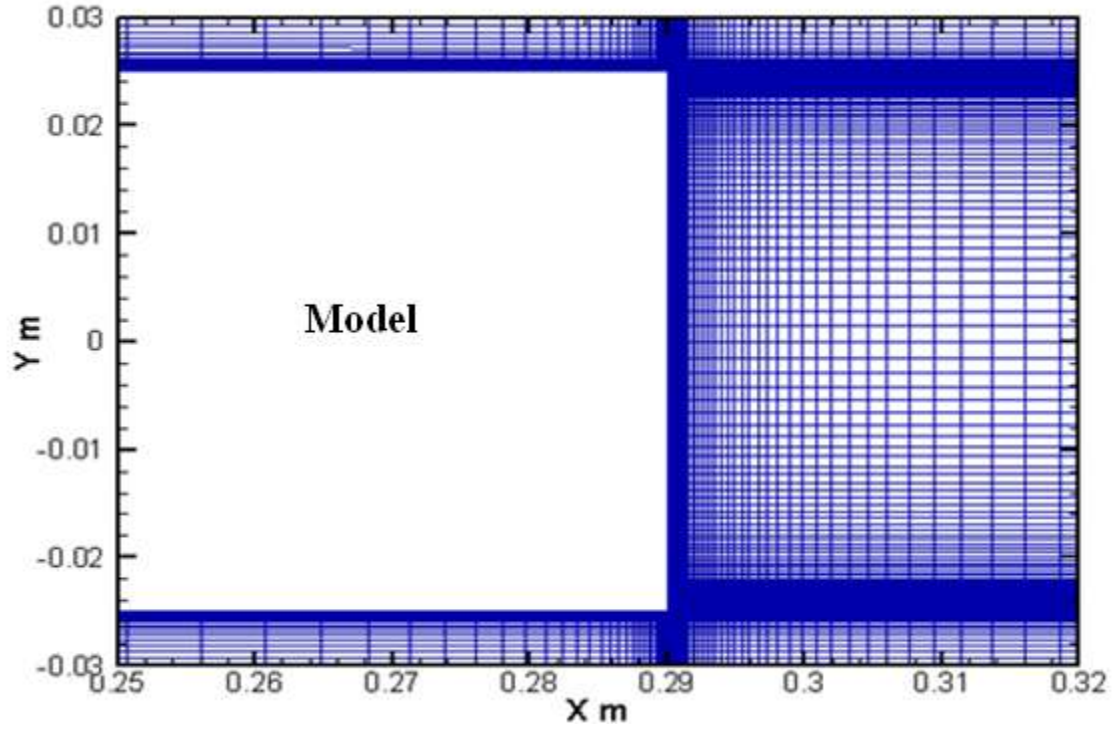

(b)

Figure 3.8 Sectional cut through the domain of the base model: (a) whole domain and (b) zoom view around the model.

Figure 3.9 shows a sectional cut through the domain of the cavity model. More cells were created around the surface of the cavity in order to represent the boundary layer around the cavity model.

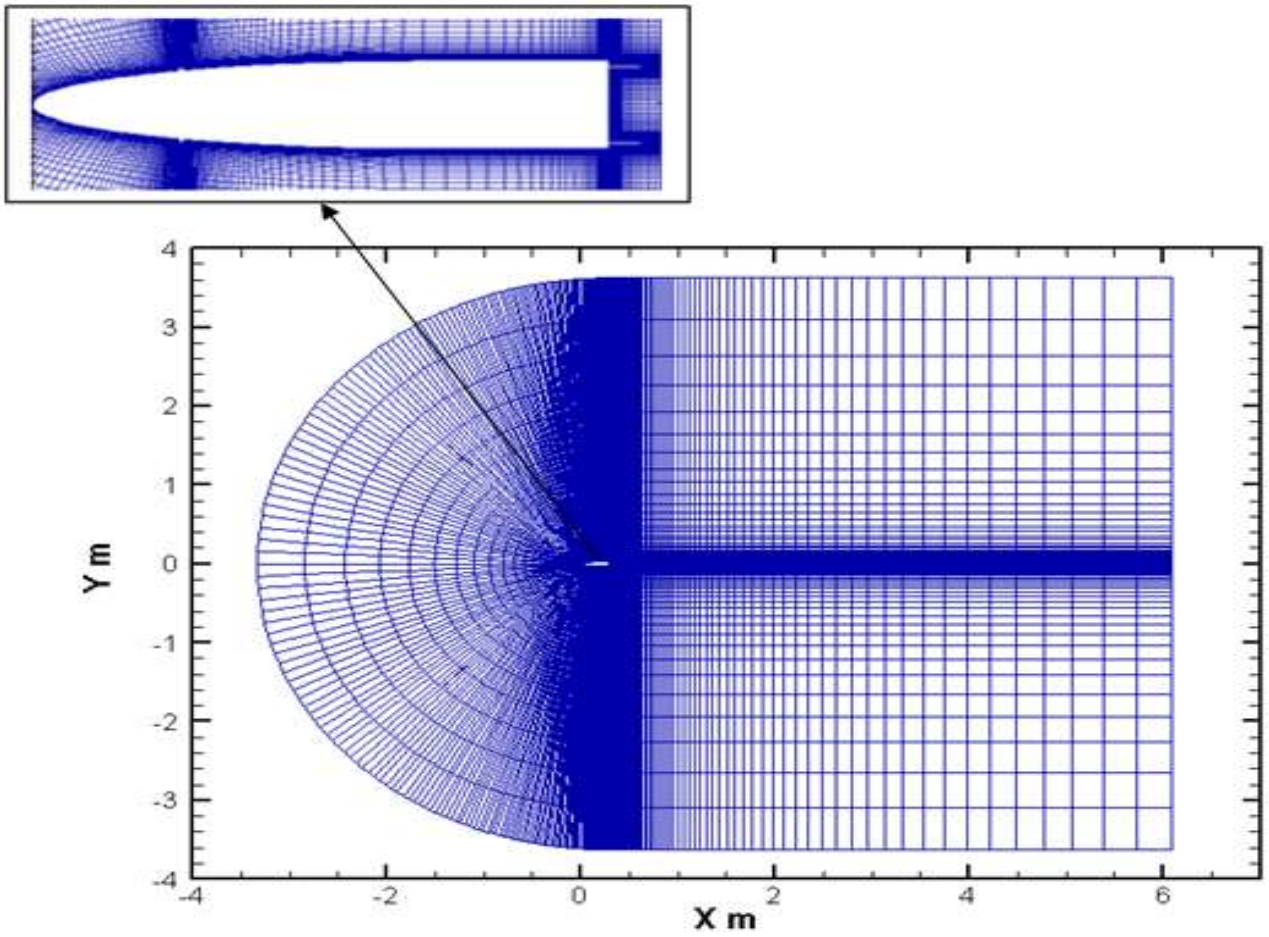

(a)

Figure 3.9 For caption see page 35.

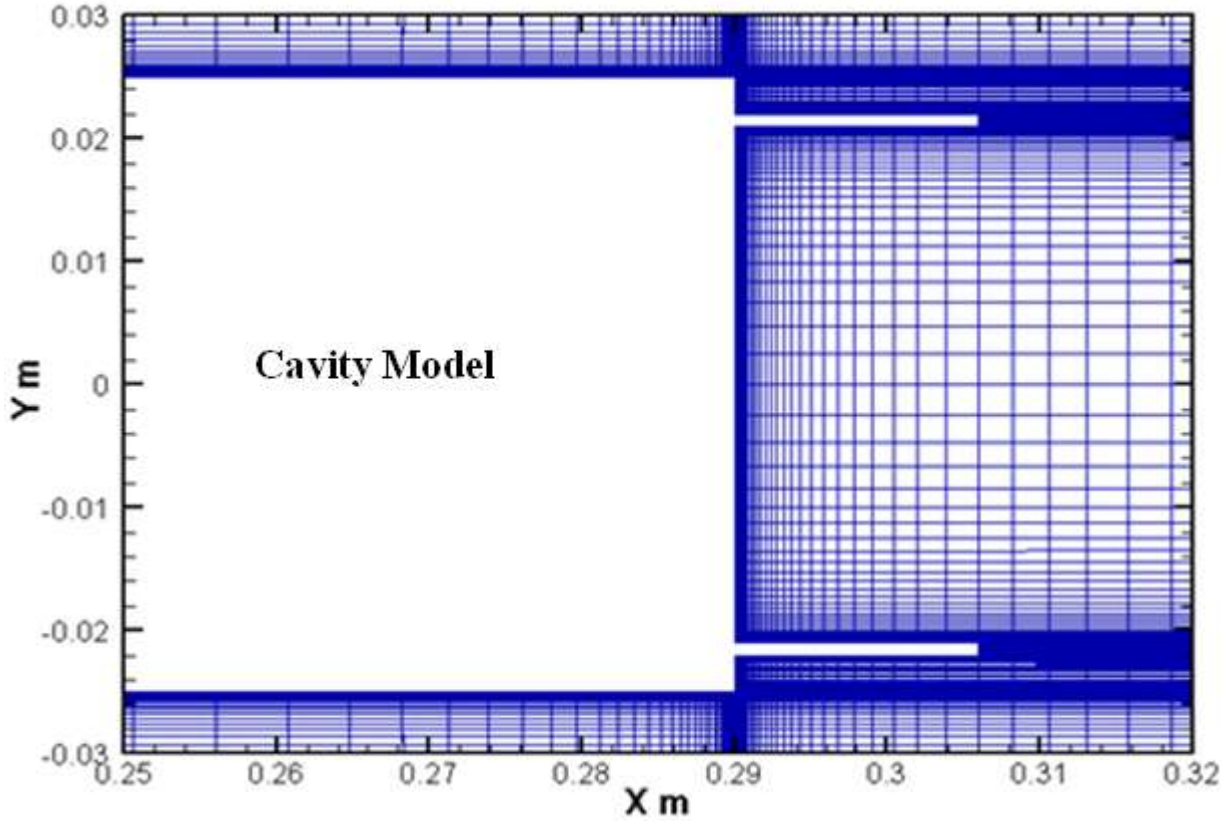

(b)

Figure 3.9 Sectional cut through the domain of the cavity model: (a) whole domain (b) zoom view around the fitted cavity.

Figure 3.10 shows a 3-D view of the computational domain and boundary conditions. It has a size of 0.7L in the spanwise directions (z-direction). The boundary conditions on the zone are velocity_Inlet at the front, top and bottom of the domain. The outlet boundary in the back side of the domain is pressure_Oulet while the rest of the boundaries (sides of the domain) are periodic.

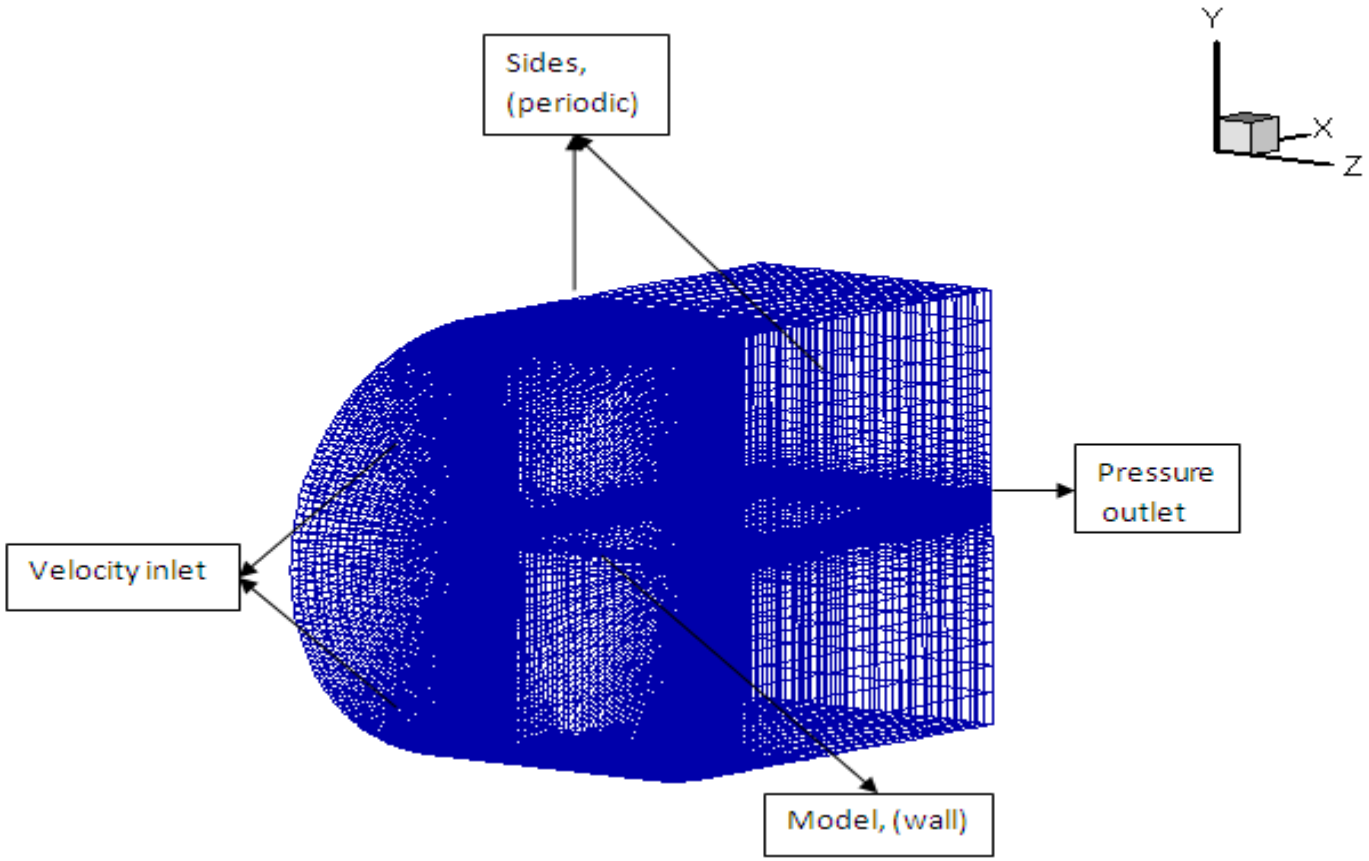

Figure 3.10 3-D view of the computational domain

3.2.4 Turbulence Modeling And Other Computational Details

The CFD simulation were conducted using RANS and LES techniques . Similar to the experiment, the computations were conducted at a Reynolds number of 2.6×10^4 based on the height of the body. LES can provide more information about the unsteady nature of the near-wake flow. In this study, subgrid-scale (SGS) turbulence was modeled using dynamic Smagorinsky model originally proposed by Germano et al.[29]. The dynamic procedure for the above finite volume solver requires a special test-filter applicable to arbitrary meshes. As illustrated example in figure 3.11, the test-filter adopted is a top-hat filter that involves the elemental volumes comprising the center cell itself plus the neighboring cells that share their cell faces with the center cell.

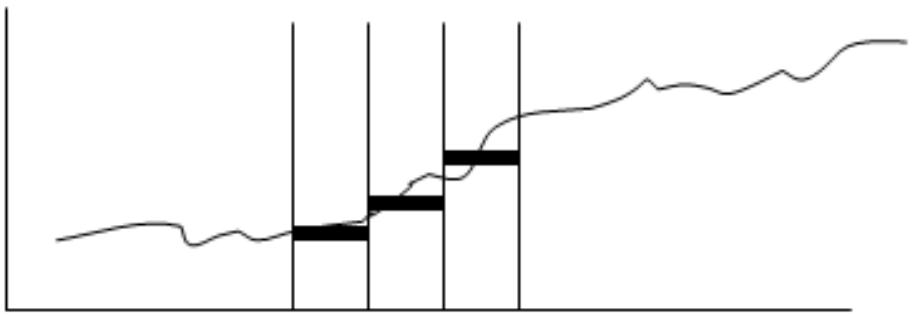

Figure 3.11 Sketch drawing illustrating the function of the top-hat filter on the arbitrary meshes.

The time step is fixed at $\Delta t = 6.4\times10^{-4}\ H/U_\infty$, giving a maximum Courant-Freidrichs-Lewy number of around 2. The number of sub-iterations per time step ranges from 10-20 , enough to reduce the momentum residual magnitude by around 3 orders of magnitude per

time step. The simulation were run for a total time of 200 H/U_{∞}. Mean quantities were sampled after a transient period of about 60 characteristic times. The sampling times were long enough to provide statistically converged quantities. The drag history was recorded. Compared to the RANS model, LES needs longer time and requires a more refined mesh to resolve the unsteady scales. Generally, LES takes 90-100 days of simulation time (1.3 million cells) compared to 2-3 days for the RANS simulation.

3.3 Grid Sensitivity Test

The current work employing various RANS turbulence models with different mesh elements for the computation of the drag coefficient around the base model to validate its accuracy as well as mesh dependency. So, the three different grids G1,G2 and G3 were created to ensure that the solution is grid-independent. The grids were made using Gambit meshing code. In RANS, Spalart-Allmaras models have been chosen to test the suitability and the applicability of the models as well as mesh dependency on the flow around the base model. As mentioned, in each grid, the size of the computational domain was kept the same and divided into four blocks. Each block is meshed separately so that the nodes could be clustered where more necessary, such as near the separation point at the leading edge and near the trailing edge. In particular it is necessary to cluster grid points near the trailing edge in order to resolve the boundary layer near the surfaces of the model.

Figure 3.12 (a) shows the first grid G1 which contains around 0.85×10^5 cells. The first row very close to the wall in order to have a value of non-dimensional wall units, y^+, around

30. The second grid G2 shown in figure 3.12 (b), contains more than 1.2×10^6 cells. More cells were created near the surfaces of the model in order to resolve the boundary layer. In G2, the first grid above the model surfaces were located in such way that the y+ is around 1. Figure 3.12 (c) shows the third grid G3 which contains around 1.7×10^6 cells. Of this number, more cells were placed in the near wake compared to G2 and G1 in order to resolve the flow structure in this region. For this grid, the y+ was the same as G2 (~1). RANS computations were performed on all the above grids while LES computation was performed on grid G2 since LES require high resolution mesh to resolve smaller scales.

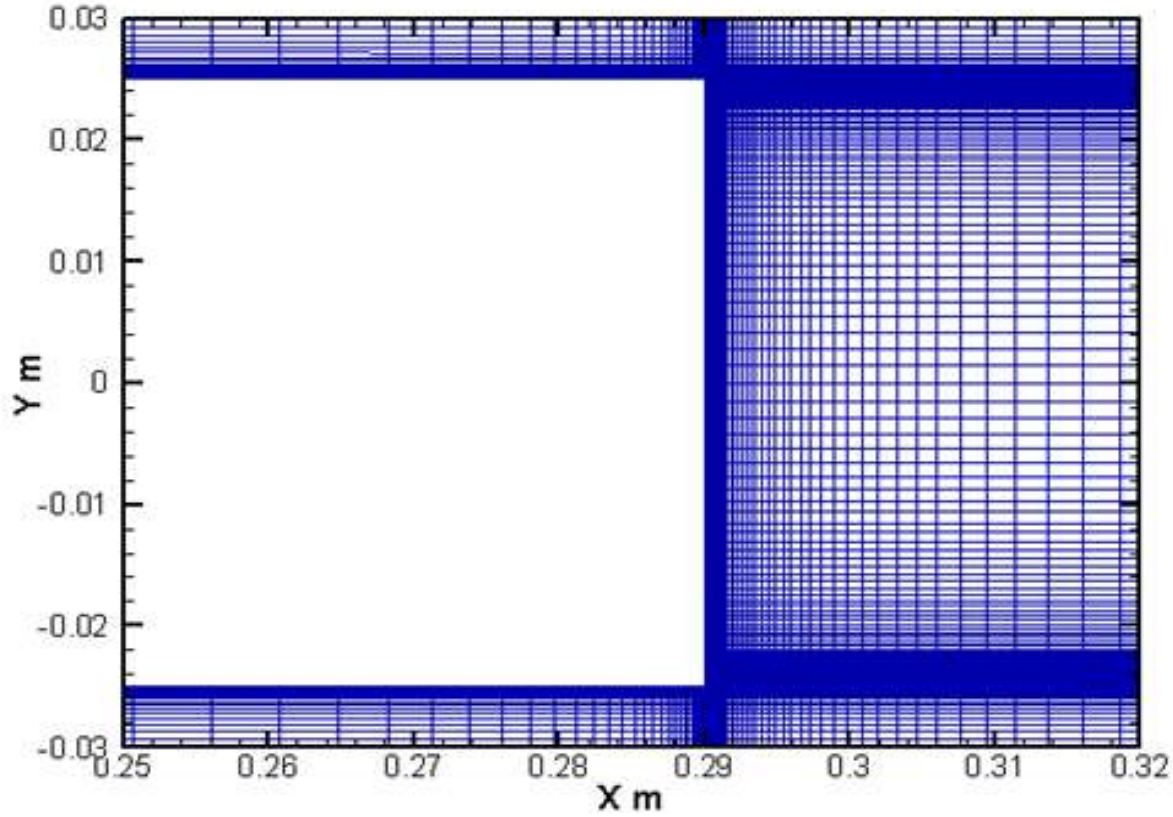

(a)

Figure 3.12 For caption see page 43.

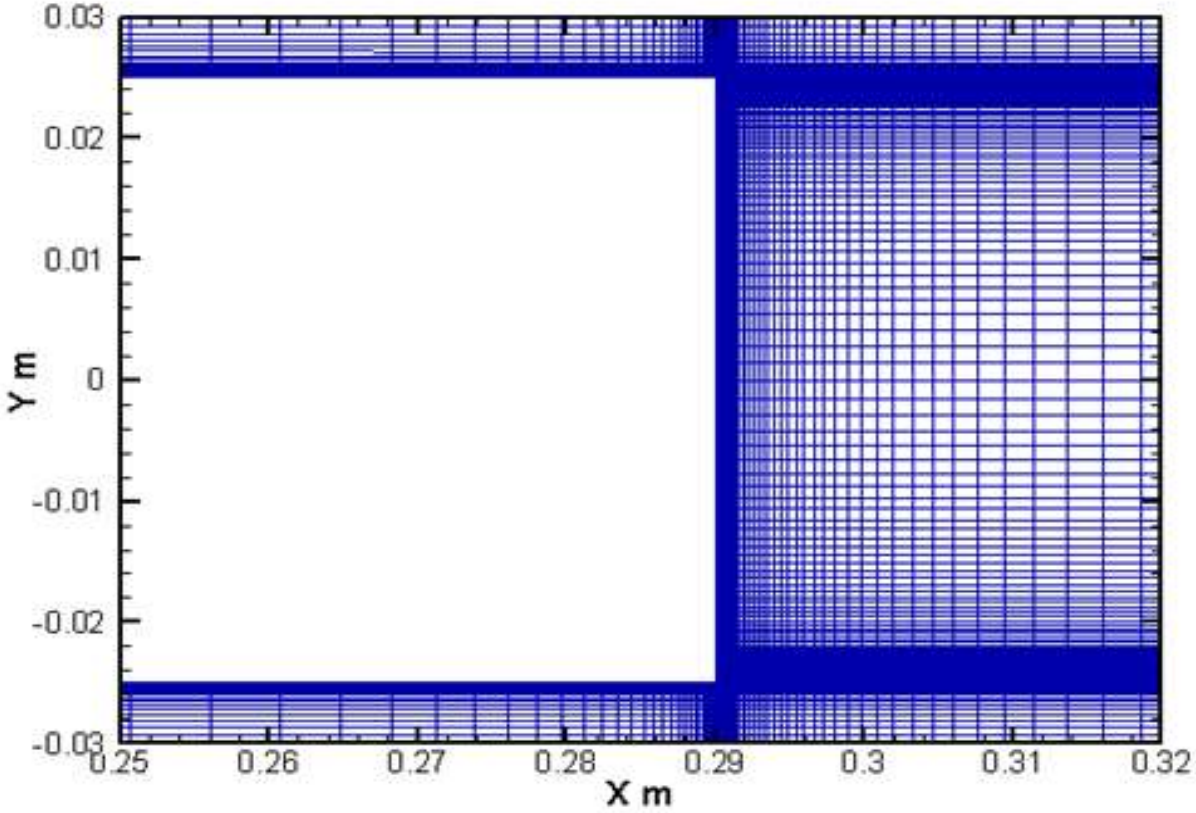

(b)

Figure 3.12 For caption see page 43.

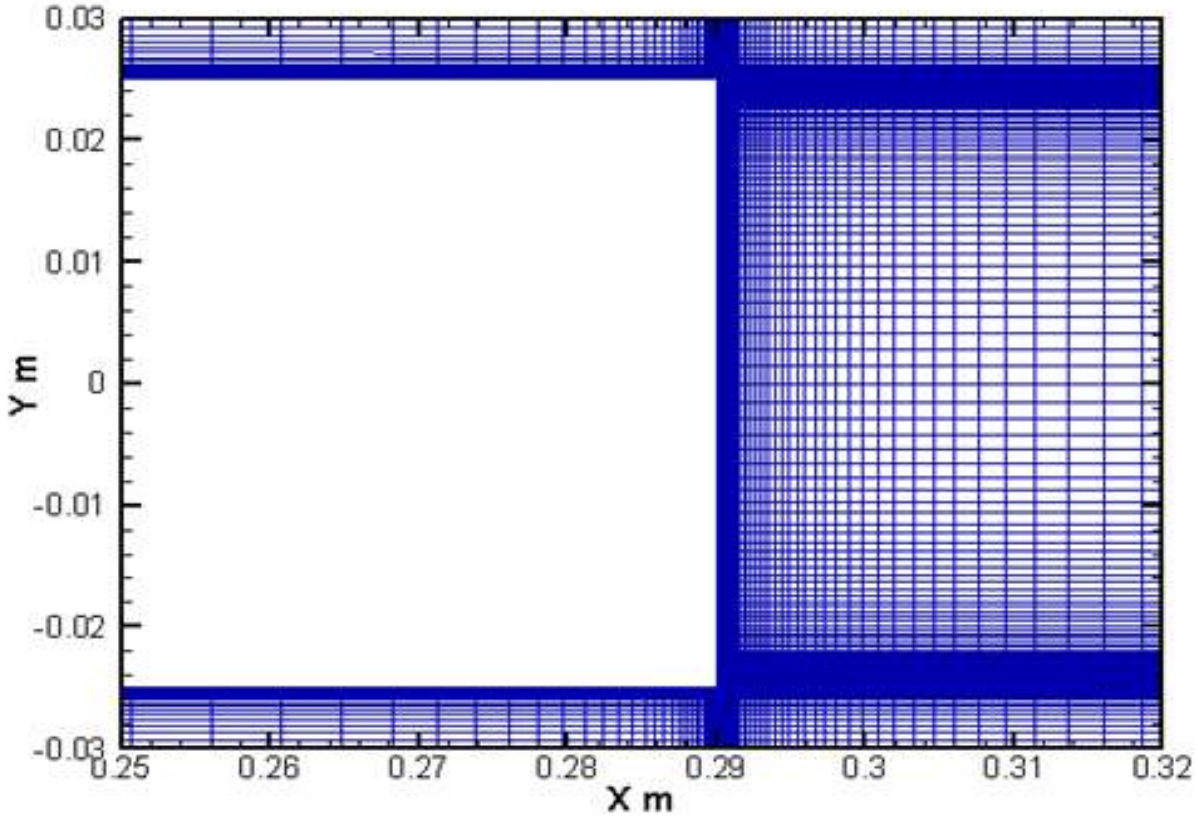

(c)

Figure 3.12 Cross-sectional view of the three grids using in grid independency test: (a) G1, (b) G2 and (c) G3.

CHAPTER 4

RESULTS AND DISCUSSION

RANS and LES computations were obtained for the base model and base model attached with 1/3h cavity at a Reynolds number of 2.6×10^4. A grid sensitivity test was conducted on the base model using three grids, namely G1, G2 and G3 containing 8.5×10^5, 1.3×10^6 and 1.7×10^6cells, respectively. The LES computation was carried out on G2 due to massive computer requirements of LES and the limitation of computer resources. This chapter is organized as follows. Section 4.1 discusses the results of the grid sensitivity test. In section 4.2, the base pressure and drag results obtained using RANS and LES, are presented. The near wake flow results of RANS and LES are discussed on section 4.3 and in section 4.4 the mean velocity profiles in the near wake region obtained using RANS and LES are presented. The CFD results were validated against experimental results in each particular section.

4.1 Results of Grid Sensitivity Test

As mentioned, the grid sensitivity tests were conducted on three grids namely G1, G2 and G3 containing 8.5×10^5,1.3×10^6 and 1.7×10^6 cells, respectively. The computations were carried out at a Reynolds number of 2.6×10^4 based on the height of the body using Spalart-Allmaras turbulence model. Figure 4.1 shows the streamlines of the mean flow at the symmetry plane in the near wake of the body for G1, G2 and G3. As can be seen, the mean flow field obtained on the three grid are exactly the same. This confirm that the solution is grid- independent.

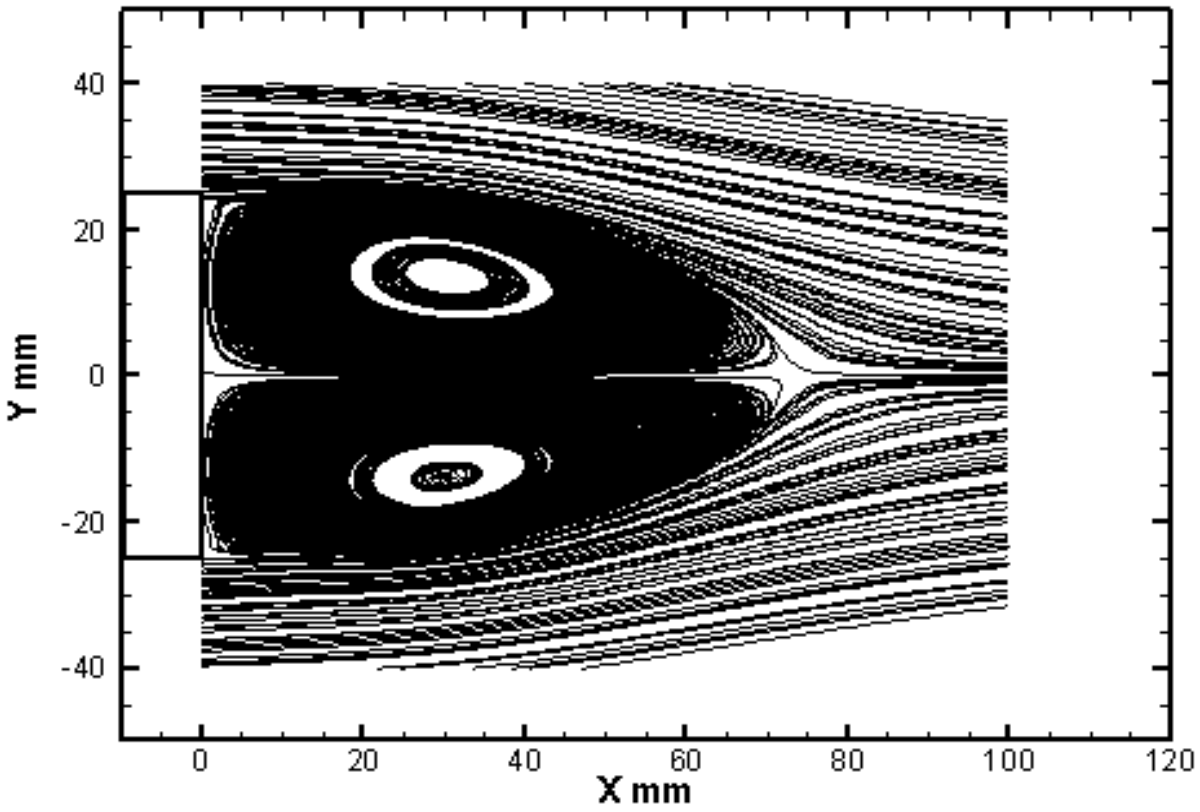

(a)

Figure 4.1 For caption see page 47.

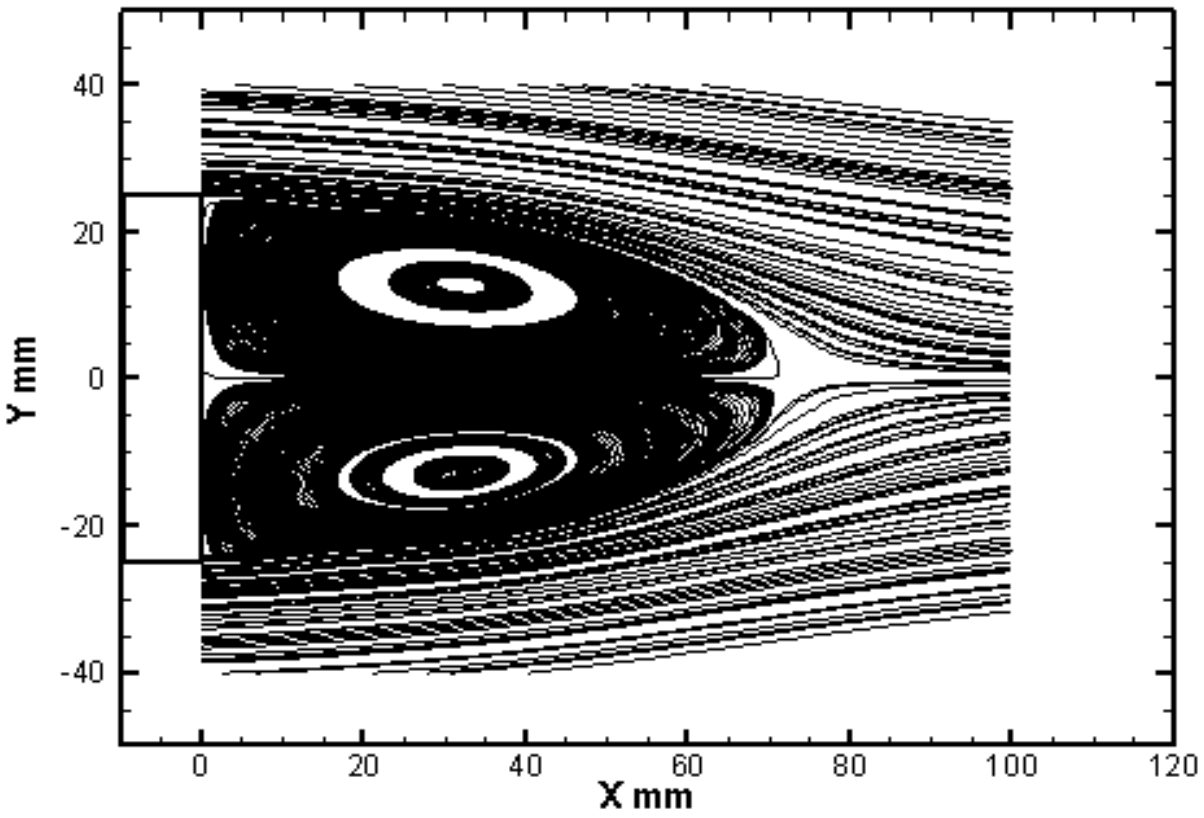

(b)

Figure 4.1 For caption see page 47.

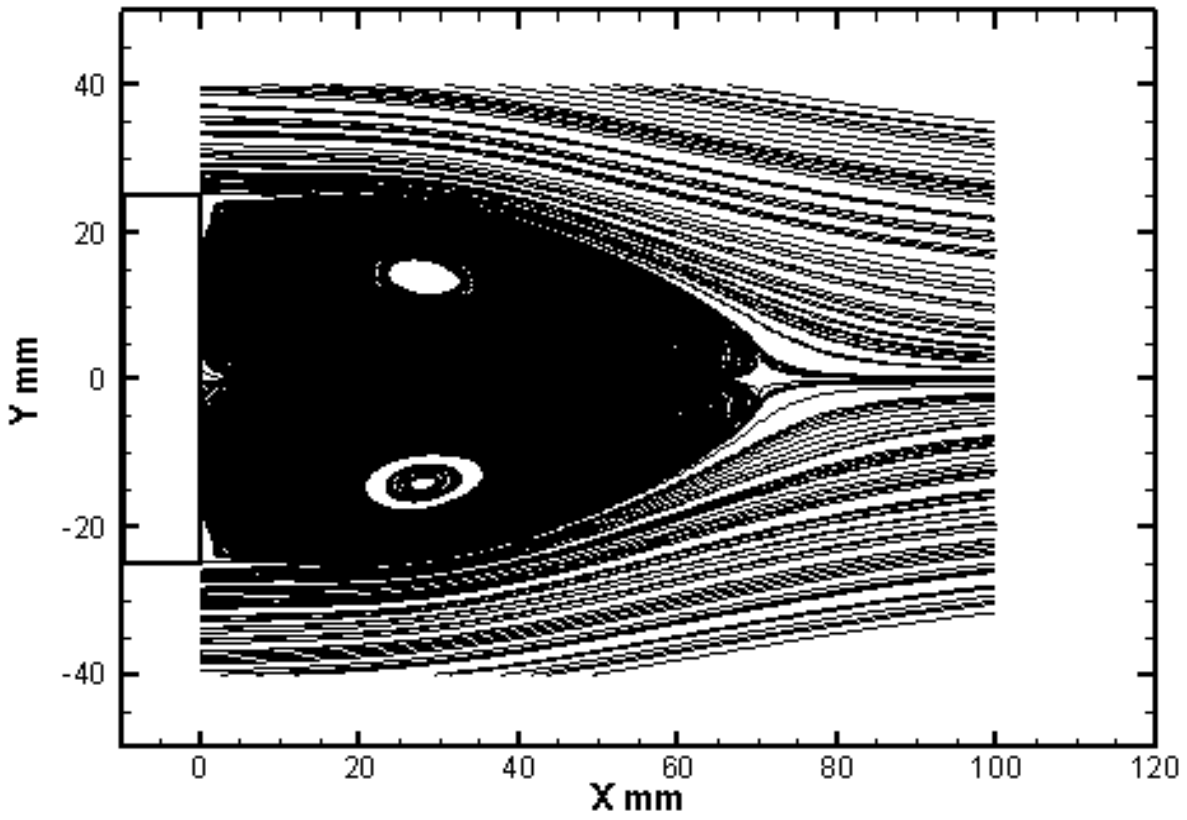

(c)

Figure 4.1 Streamlines of the mean flow at the symmetry plane using RANS: (a) G1, (b) G2 and (c) G3.

Figure 4.2 shows the velocity vector fields of the mean flow superposed with contours of the mean z-vorticity field at the symmetry plane for the three grids G1,G2 and G3. The figure shows the shear layer originating from the top and bottom sides of the body. Again, all three grids produced the same flow field.

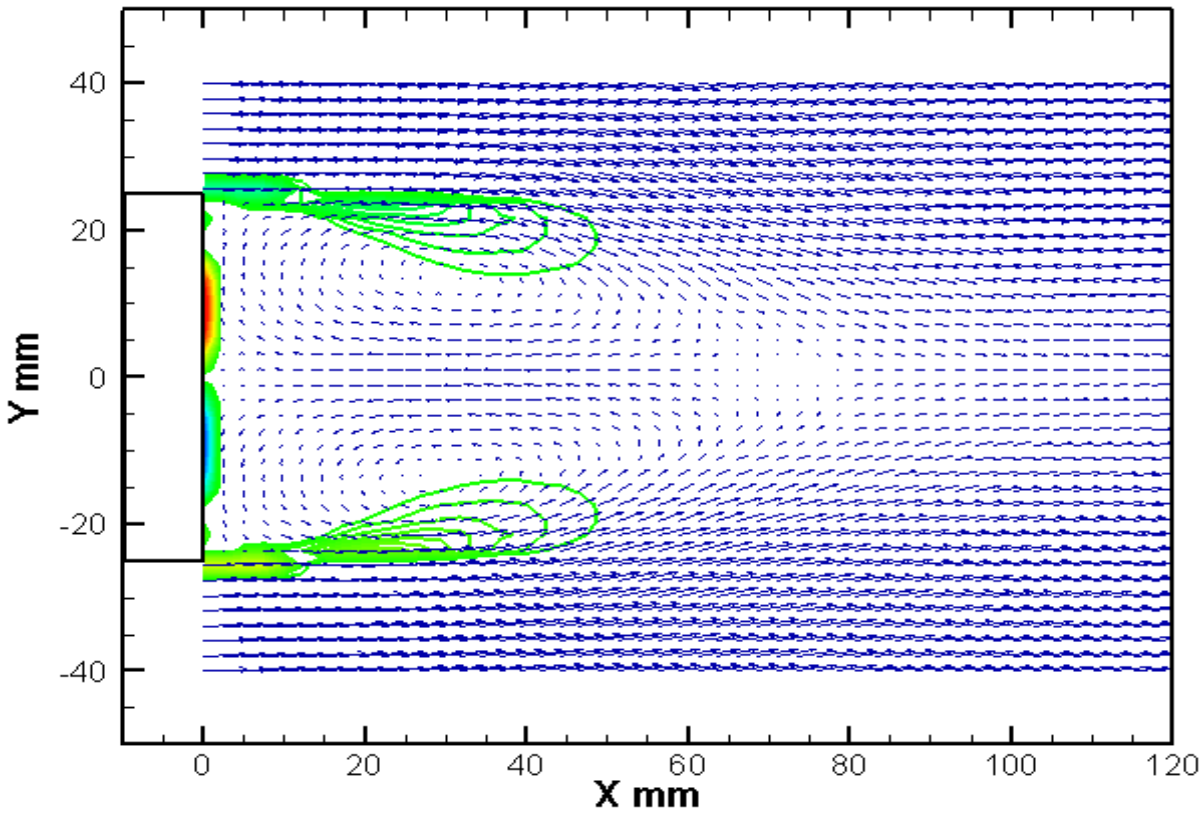

(a)

Figure 4.2 For caption see page 51.

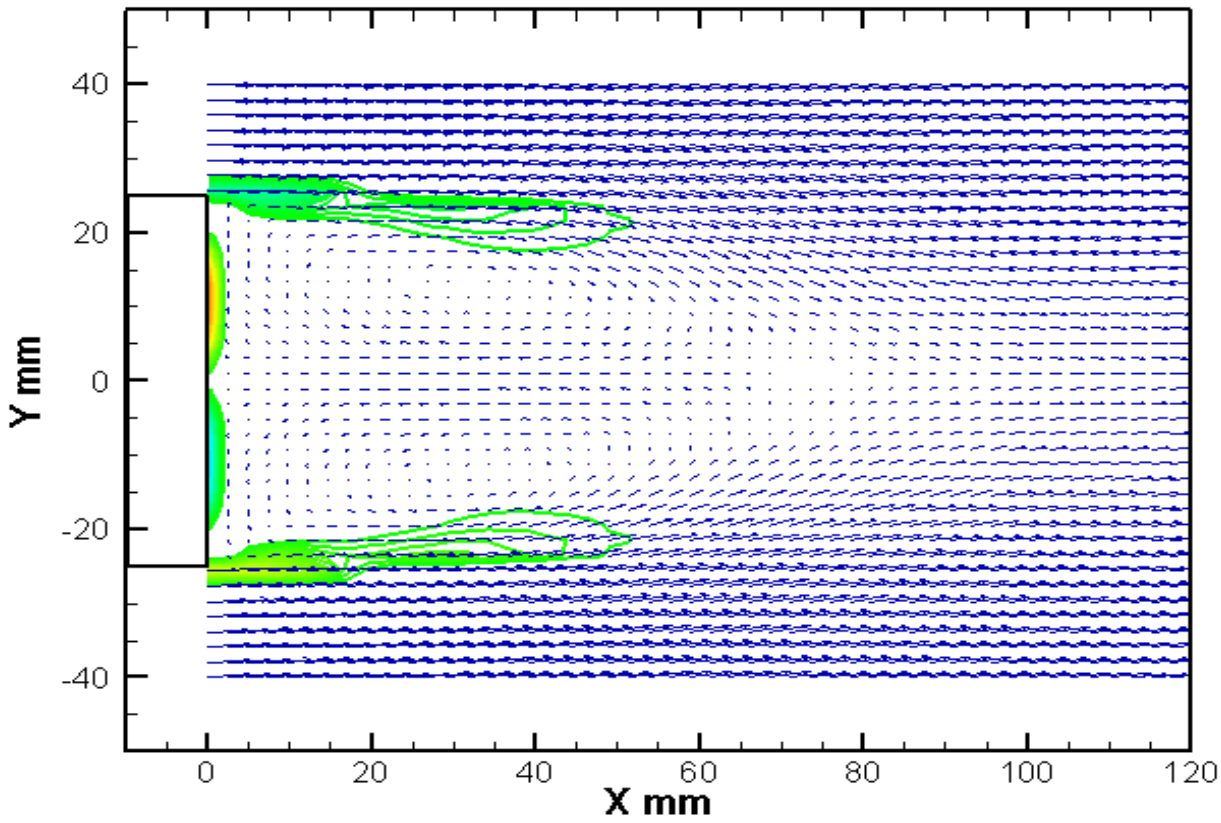

(b)

Figure 4.2 For caption see page 51.

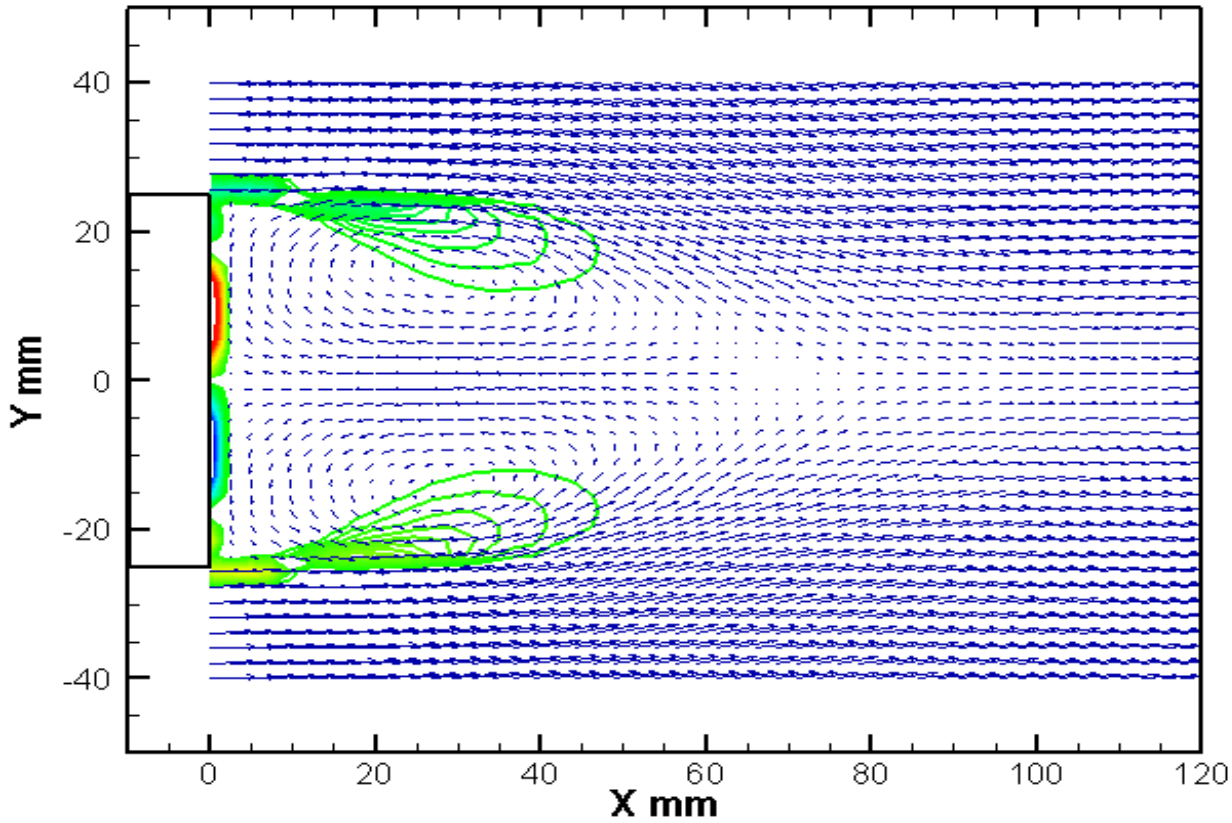

(c)

Figure 4.2 Velocity vector and vorticity contours using RANS: (a) G1, (b) G2 and (c) G3.

A more careful examination of the results obtained with the above grids is to compare the base pressure coefficient distribution and the drag coefficient. The base pressure coefficient distributions obtained on the three grids are shown in figure 4.3 where C_p are -0.37, -0.39 and -0.41 for G1, G2 and G3 respectively. The figure shows that the spanwise base pressure distributions for all grid are nearly the same. Moreover, table 4.1 lists the drag coefficients for the three grids. For G1, the drag coefficient is 0.552 compared with 0.562 for G2 and 0.574 for G3. The percentage difference between G1, G2 and G3 is very small (less than 4%). Based on the above results, it can be said that the solution is grid-independent.

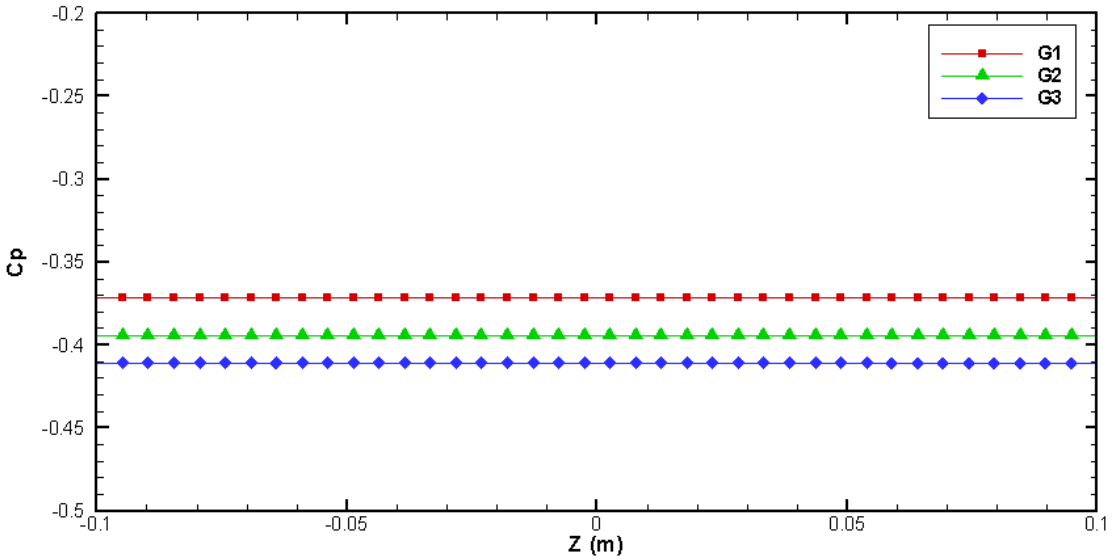

Figure 4.3 Spanwise base pressure distribution obtained on the three grids using RANS.

Method	Drag coefficient C_D
Grid G1	0.552
Grid G2	0.562
Grid G3	0.574

Table 4.1 Drag coefficients obtained on grid G1,G2 and G3 using RANS computation

4.2 Base Pressure Distribution

4.2.1 Base Model

Figure 4.4 shows the spanwise base pressure coefficient distribution for the base model computed using RANS and LES. The figure also shows the experimental base pressure obtained by ChandraMohan [30]. As can be seen, the RANS over predicted the base pressure (C_p~-0.4) compared with experimental. For the LES, however, the pressure distribution obtained was lower than experimental and C_p ranges from -0.6 to -0.7. This shows that LES prediction is better than RANS prediction and the use of LES will improve the prediction of aerodynamic forces.

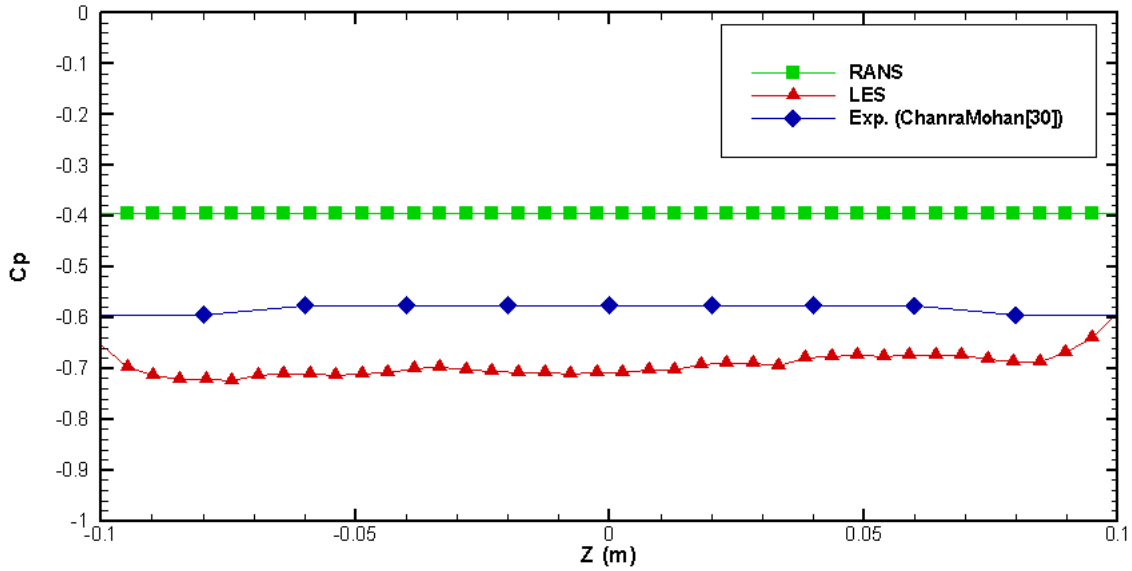

Figure 4.4 Base pressure distribution across spanwise direction for the base model using RANS,LES and experiment([30]).

4.2.2 Base Model fitted with 1/3 h cavity

Figure 4.5 shows the spanwise pressure distribution obtained using RANS and LES for the base model fitted with 1/3h cavity. Also, the experimental pressure distribution is shown in the same figure for direct comparison. The C_p obtained with LES is almost constant along the span(C_p~-0.31) is in excellent agreement with experimental values(C_p~-0.316). For the RANS, the pressure coefficient is also constant along the spanwise direction(C_p~-0.29). This shows that RANS and LES have predicted the base pressure distribution with excellent accuracy.

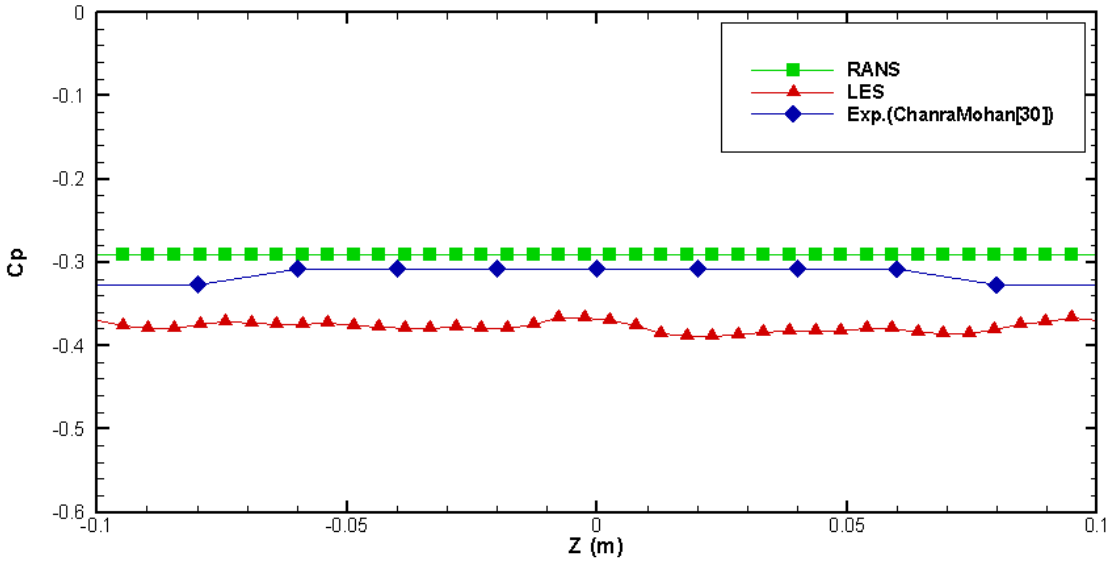

Figure 4.5 Base pressure distributions across spanwise direction for 1/3 h cavity obtained with RANS, LES and experiment([30]).

The mean pressure coefficients obtained at the center of the base for the reference model and the 1/3 h cavity using RANS, LES and experiment are tabulated in Table 4.2. For the base model, the mean pressure coefficients obtained with RANS and LES are -0.39 and -0.56, respectively. When comparing these values with experimental pressure coefficient which is nearly -0.58, the differences are around 32% for RANS and 3% for LES. This shows that RANS fails to predict the base pressure. Hence, pressure will lead to inaccurate aerodynamic force prediction and that the LES is an excellent tool to predict the flow around bluff bodies. For the base fitted with 1/3 h cavity, the mean pressure coefficients obtained with RANS, LES and experiment are -0.29 and -0.316 and -0.31, respectively. The accuracy of the LES is within 2% compared to around 6% for the RANS. It can be seen that the differences between RANS and LES is not as large as for the base model fitted with the cavity.

Model	C_p (RANS)	C_p (LES)	C_p (Exp.[30])	Percentage Error
Base model	-0.39	-0.56	-0.58	32 % (RANS) 3.4 % (LES)
1/3 h cavity	-0.29	-0.316	-0.31	6 % (RANS) 1.9 % (LES)

Table 4.2 Base pressure coefficients at the center for the base model and model with fitted 1/3 h cavity using RANS, LES and experiment([30]).

4.3 Drag

Figures 4.6 shows the time history of the drag coefficient for the base model using LES. The drag coefficient is plotted against non-dimensional time units, tU/H. As can be seen, the flow reaches almost statistically steady after almost 80 time units (one time unit = U/H). After this time, data were collected to compute the mean flow parameters for almost 120 time units. The mean drag coefficient is found to be around 0.65 which is in good agreement with experimental drag coefficient which is around 0.61 [30].

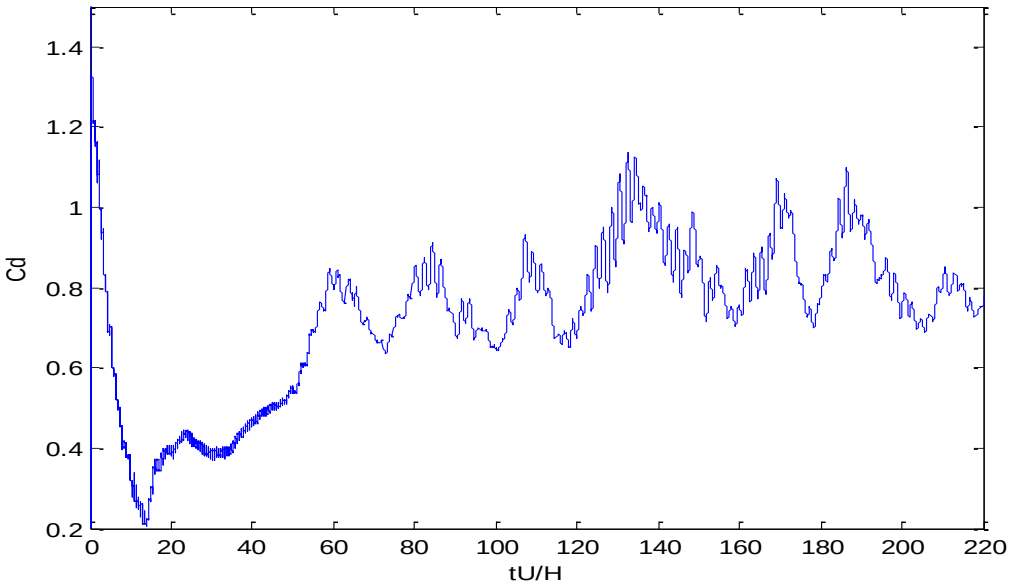

Figure 4.6 Time history of drag coefficient of the flow around base model at the center.

Figures 4.7 shows the time history of the mean drag coefficient for the base model fitted with 1/3h cavity using LES. Similar to the base model, the drag coefficient is plotted against non-dimensional time units tU/H. The flow was simulated for 160 time unit enough to get good statistic of the mean flow. The sampling was started after 40 time units. From the figure, the mean drag coefficient is around 0.37 which is in excellent agreements with ChandraMohan experiment results where the drag coefficient is about 0.35,[30]. Moreover, the figure shows that drag coefficient is reduced using 1/3h cavity by around 43 % comparing to the base model without cavity attached.

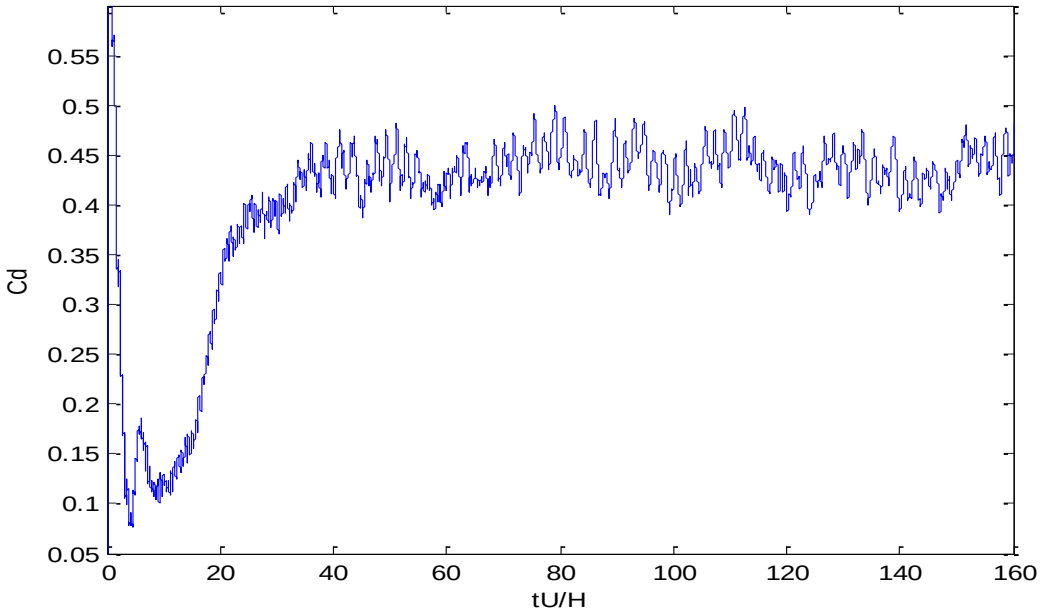

Figure 4.7 Time history of drag coefficient of the flow around base model fitted with 1/3h cavity at the center.

The mean drag coefficients for the base model and the model fitted with 1/3 h cavity obtained using RANS,LES and experiment are tabulated in Table 4.3. The mean drag coefficients for the base model using LES model is around 0.65 while the base model with fitted 1/3 h cavity is 0.37 which showed a drag reduction as well as good agreement with experimental data. On the other hand , the RANS under predicted the drag coefficient by around 7.8% for base model and 34% for the cavity model. These results along with the previous results shows that LES is better in productivity the flow around these geometries.

Model	C_d (RANS)	C_d (LES)	C_d (Exp.[30])	Percentage Error
Base model	0.562	0.65	0.61	7.8 % (RANS) 6.5 % (LES)
Base model with 1/3 h cavity	0.471	0.37	0.35	34% (RANS) 5.7 % (LES)

Table 4.3 Comparison of simulated and measured drag coefficient for the base model and model fitted with 1/3h cavity using RANS, LES and experiment([30]).

4.4 Near Wake Flow

4.4.1 Base Model

A typical instantaneous flow field in the vertical symmetry plane of the near wake of the base model is shown in figure 4.8. The figure shows a normal vorticity contours superposed on the instantaneous velocity vector field. As expected the shear layer originates at the upper and lower edges of the base model. The shear layer originating from the upper edge has a negative z-rotation while the shear layer originating from the lower side has positive z-rotation. These shear layers break into small vortex structures in manner similar to the Von Kármán vortex street. The upper flow rotates more rapidly toward the center of the wake which in turn pushes the underbody flow further downstream and this continues in alternating manner between the underbody and upper flow . This figure shows that although the flow is mainly two dimensional, it is very complex and highly unsteady.

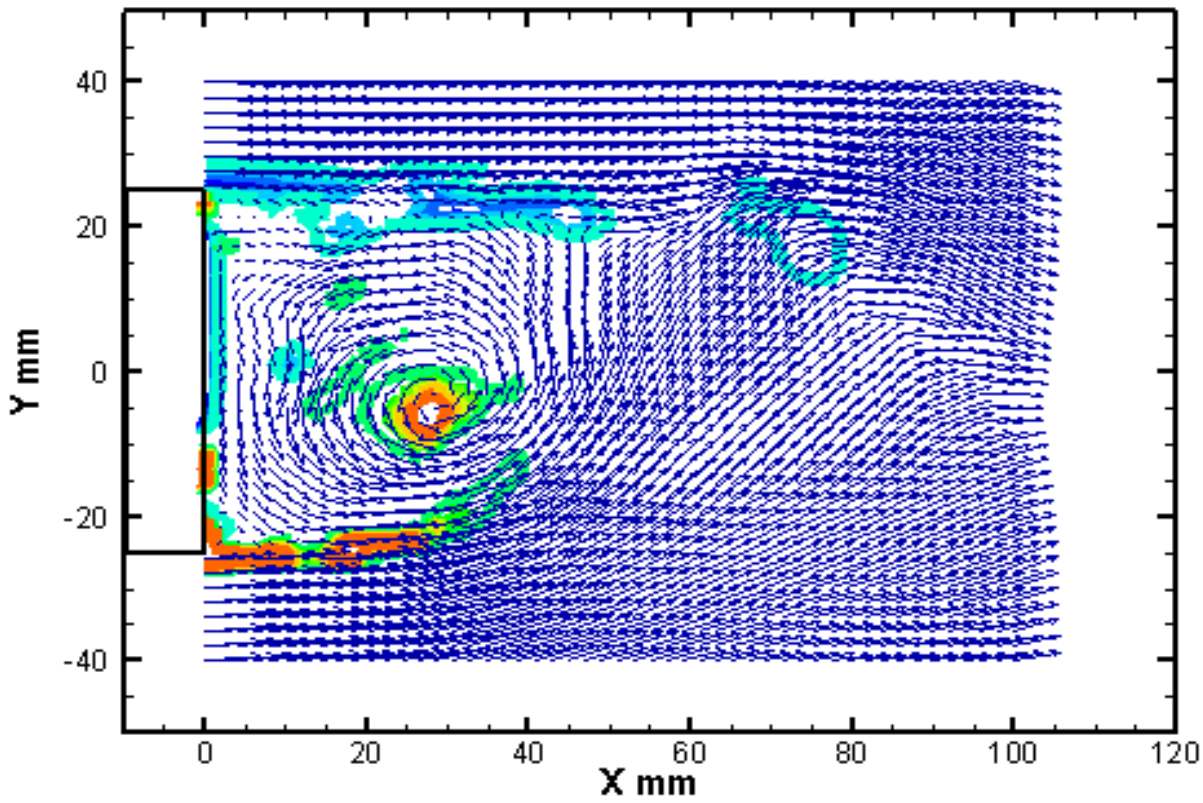

(a)

Figure 4.8 For caption see page 62.

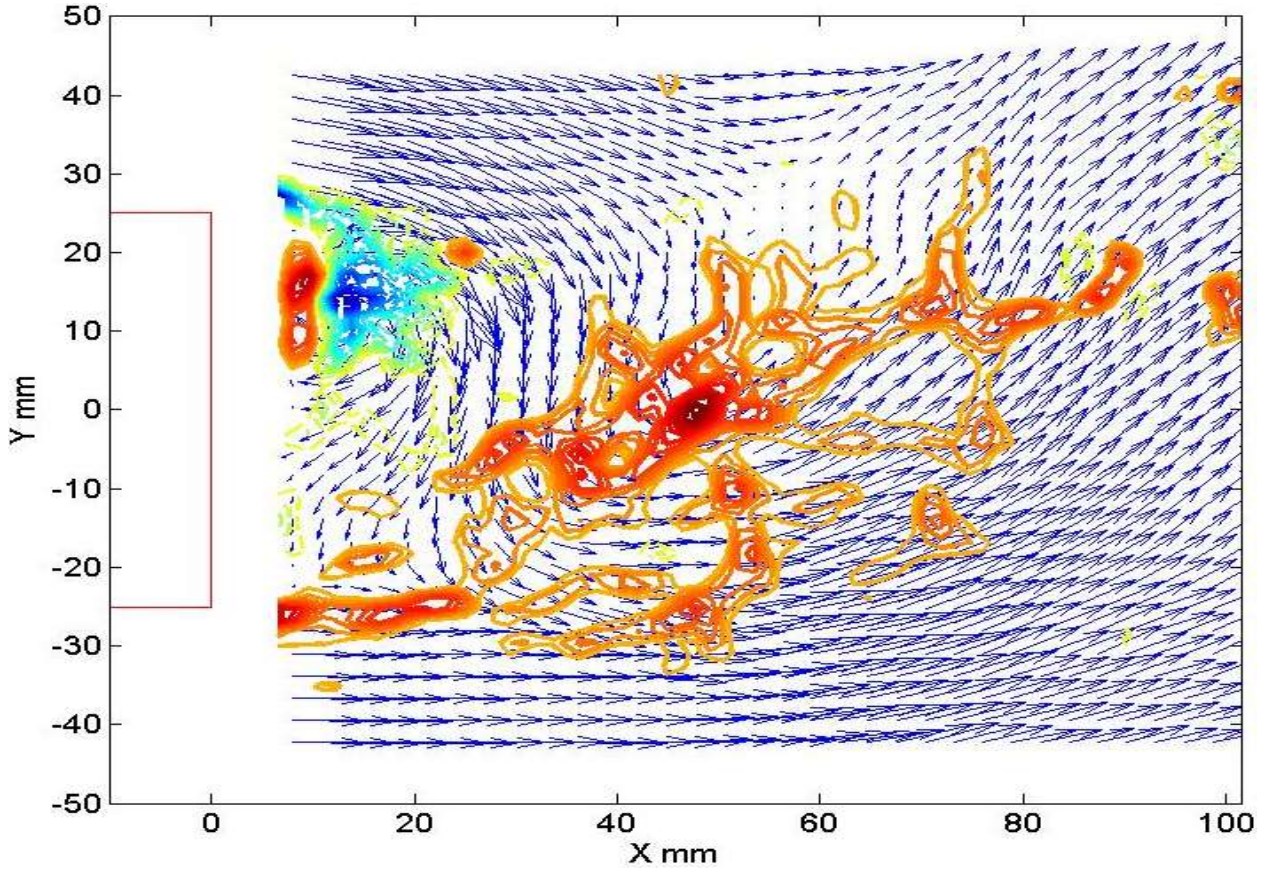

(b)

Figure 4.8 Instantaneous velocity and vorticity fields in the symmetry plane of the base model: (a) LES and (b) experiment ([30])

Figures 4.9 shows the vector plot of mean velocity field obtained using RANS, LES and experiment. Both the RANS and LES predicted two recirculation regions behind the model. However, as shown in Figure 4.9(a) the location of the recirculation regions predicted by RANS is further downstream when compared with LES or experiment. Figure 4.9(b) shows that the LES mean flow field is in excellent agreement with the experimental mean flow field (Figure 4.9(c)).

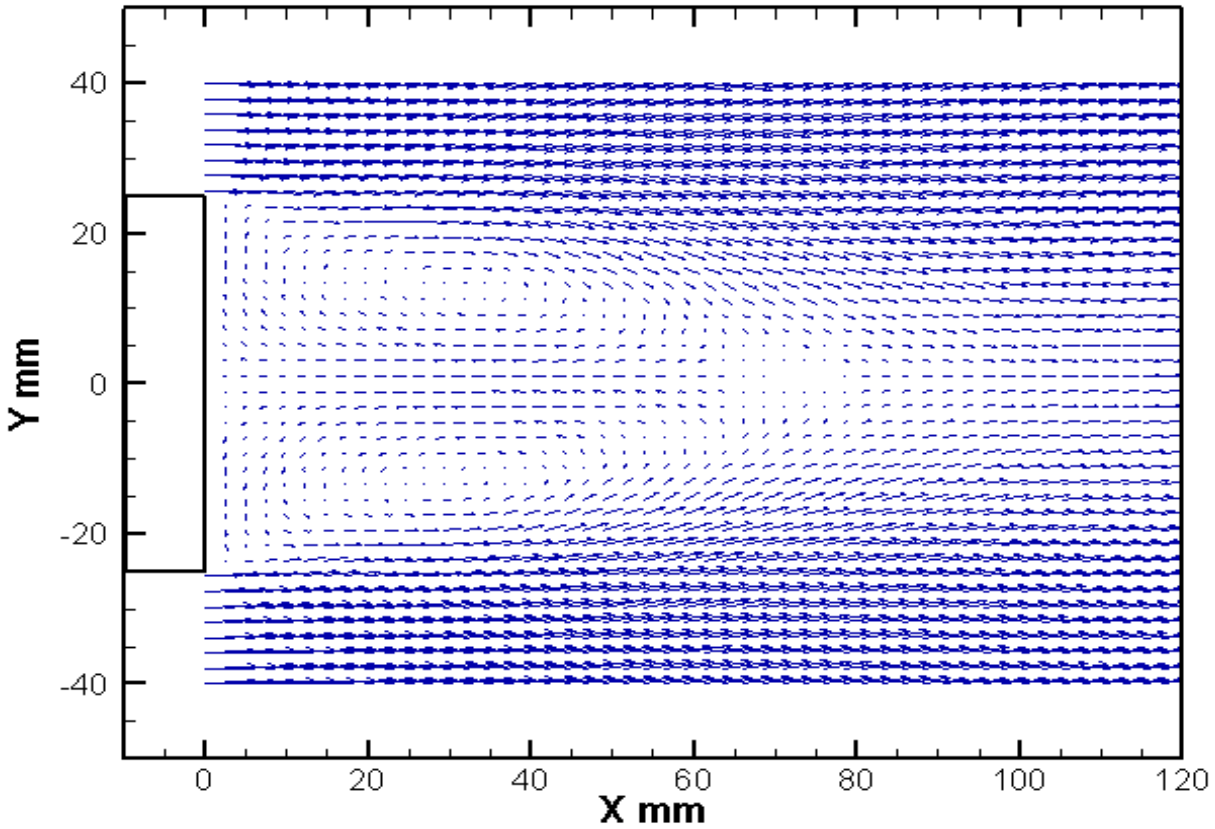

(a)

Figure 4.9 For caption see page 66.

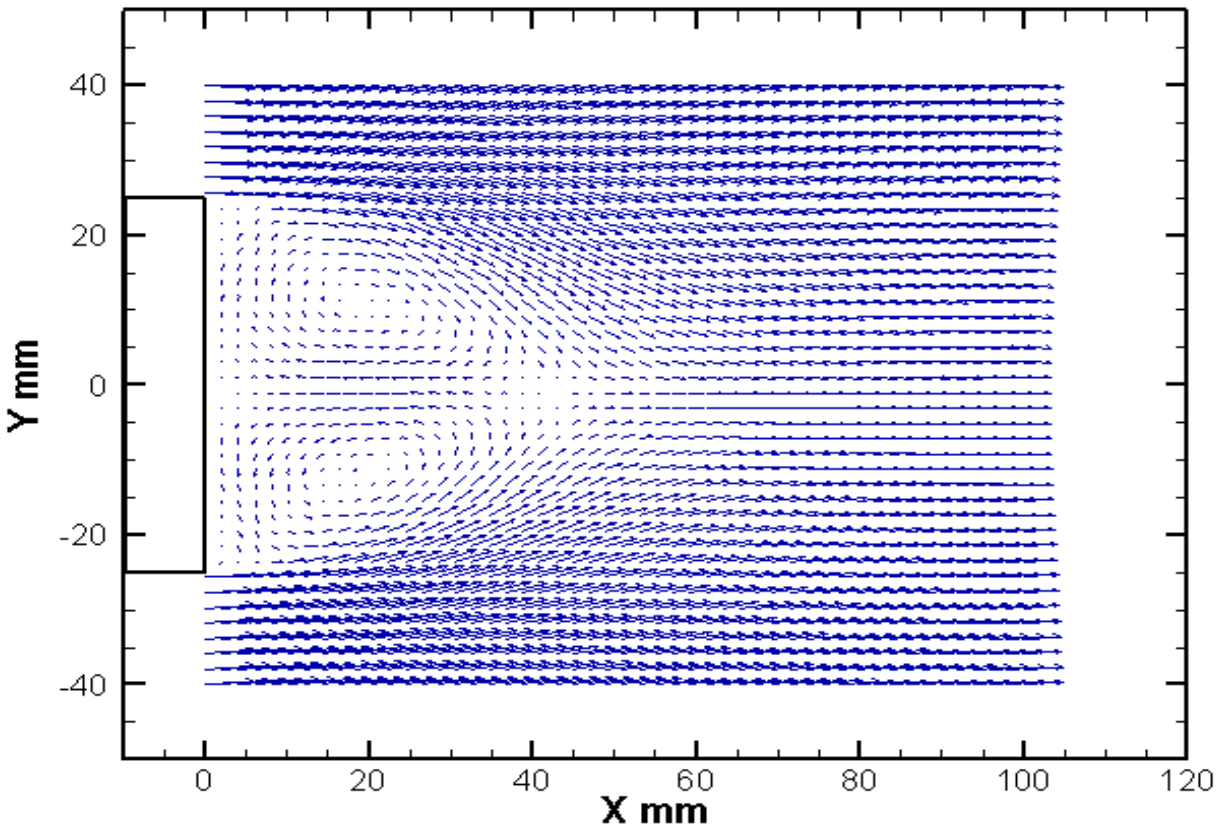

(b)

Figure 4.9 For caption see page 66.

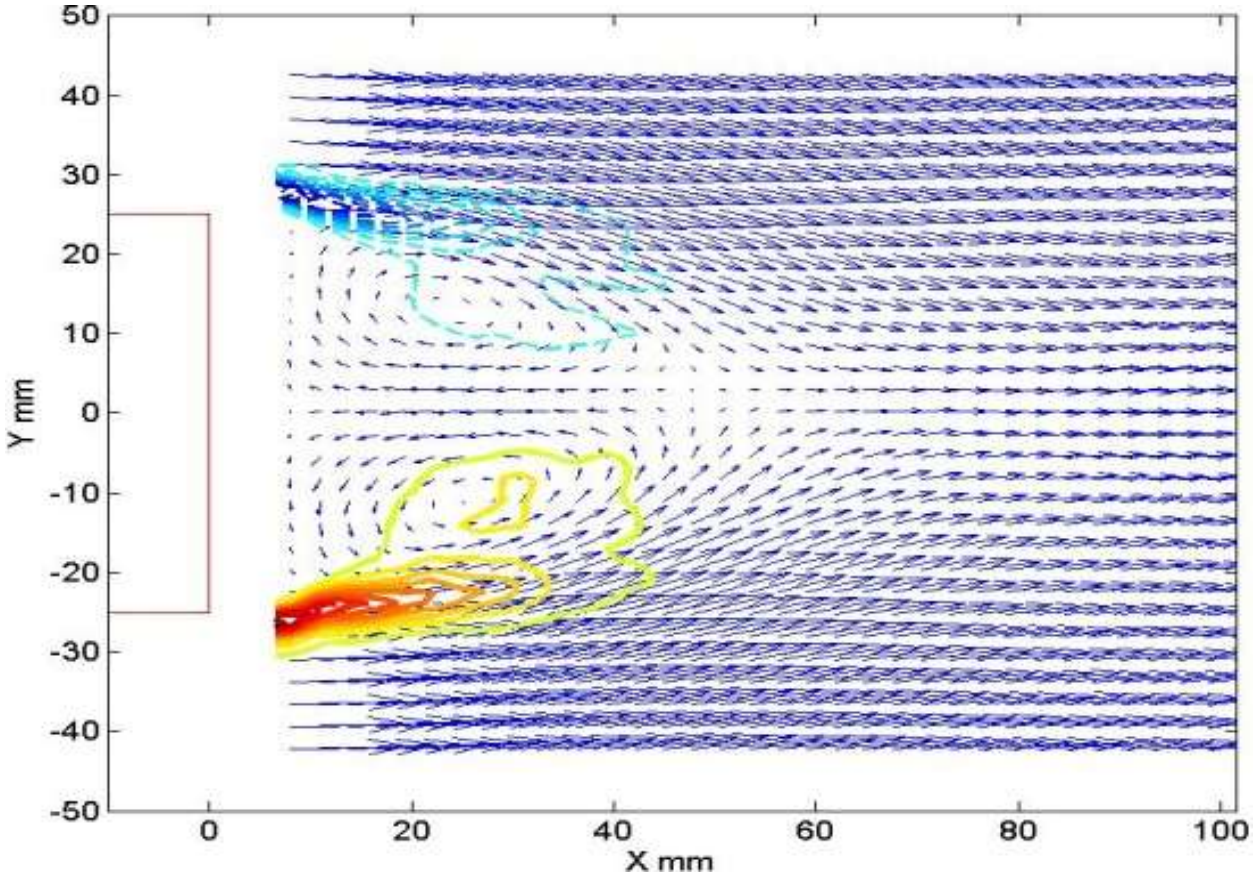

(c)

Figure 4.9 Mean velocity in the symmetry plane of the base model: (a) RANS, (b) LES, (c) experiment ([30])

Figures 4.10 show streamlines of the mean velocity field at the symmetry plane in the near wake of the base model obtained using RANS, LES and experiment. The length of the recirculation region, L_R, is around 80 mm for the RANS and 50 mm for the LES. This shows a 66% difference for RANS and 4.2% for the LES when compared with experiment (L_R= 48 mm). This shows that LES method is better than RANS method not only in predicting pressure distribution but also in predicting of the near wake flow.

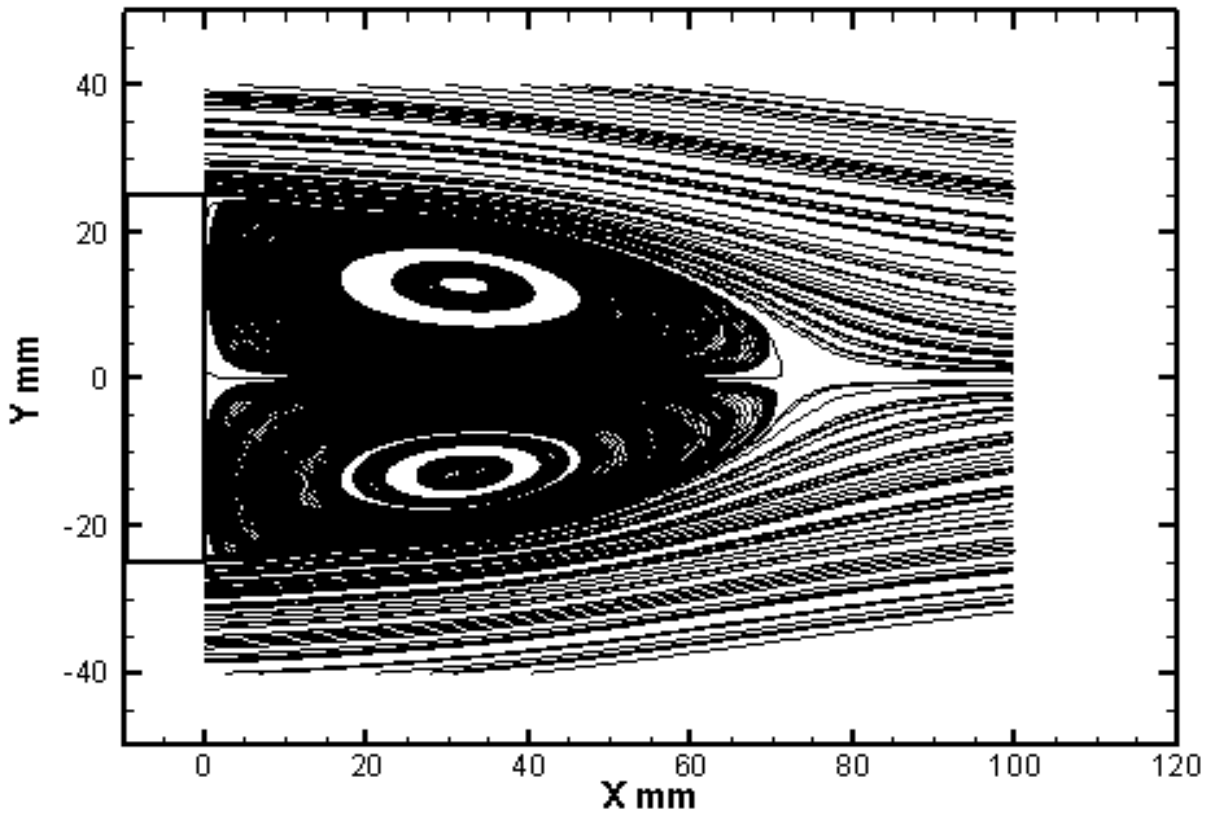

(a)

Figure 4.10 For caption see page 70.

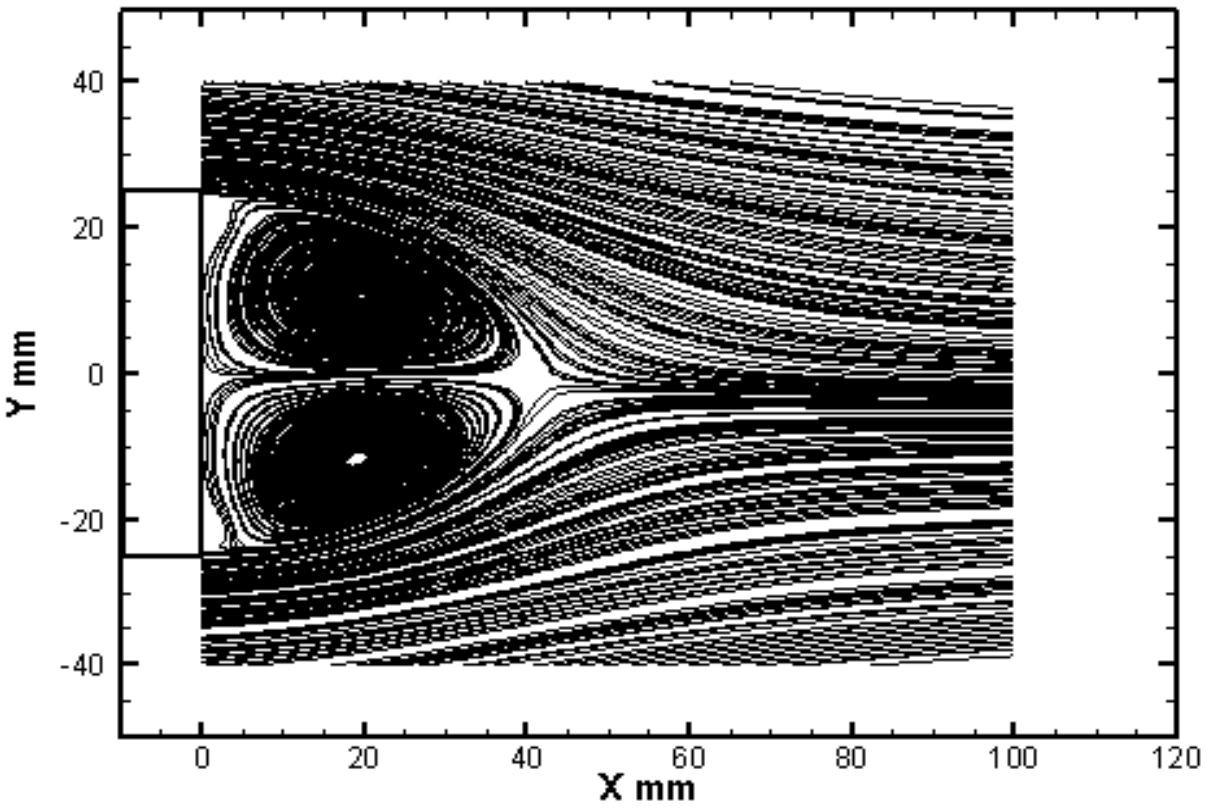

(b)

Figure 4.10 For caption see page 70.

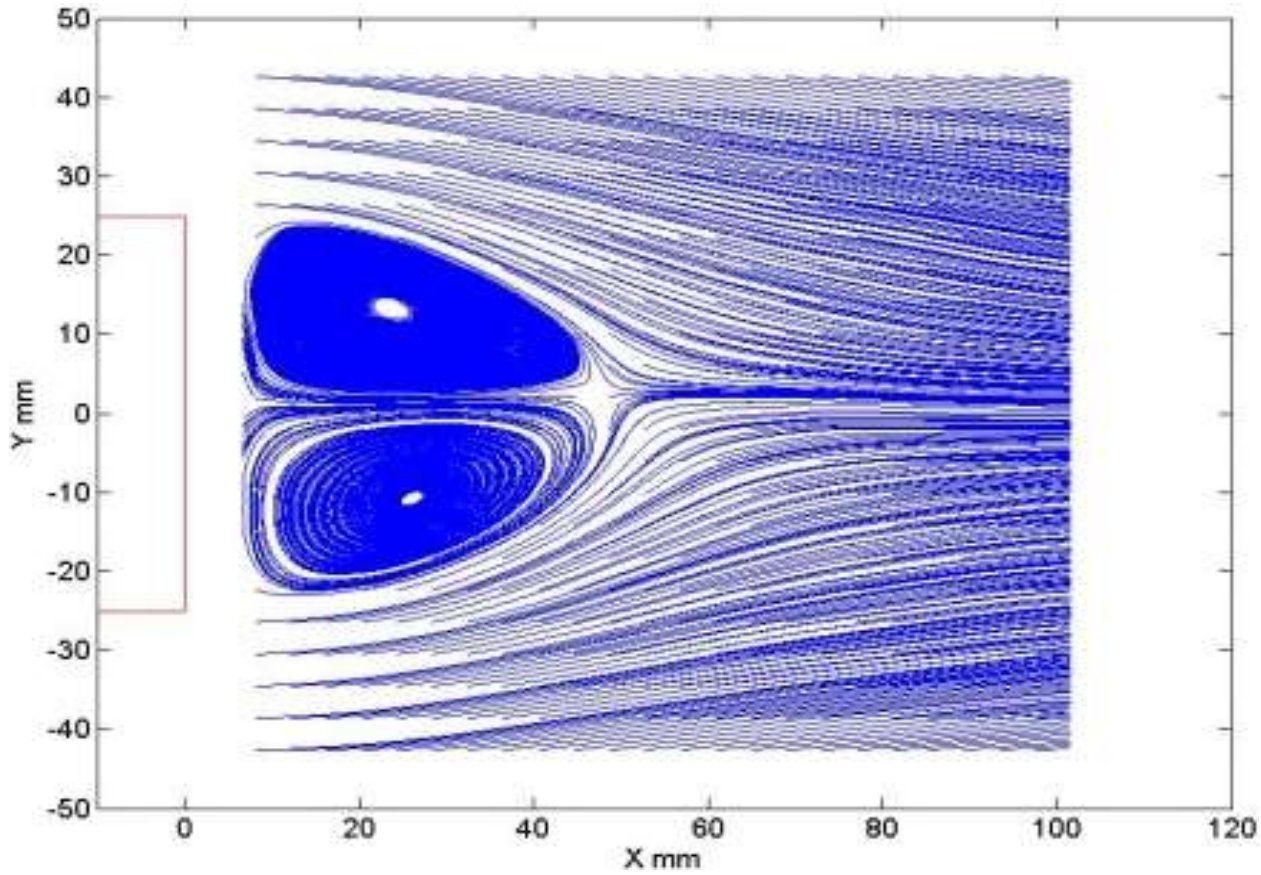

(c)

Figure 4.10 Streamlines of the mean velocity field in the symmetry plane of the base model: (a) RANS, (b) LES, (c) experiment ([30])

4.4.2 Base model fitted with 1/3 h cavity

A typical instantaneous flow field in the vertical plane is shown in figure 4.11 for the model fitted with 1/3h cavity using LES method. The figure shows a normal vorticity contours superposed on the instantaneous velocity vector field. As can be seen in figure 4.12(a), two shear layers originate from the upper and lower surfaces of the base model and interact with shear layers developed at the upper and lower edges of the cavity Again, the shear layer originating from the upper edge has a negative rotation around z-axis while the shear layer originating from the lower side has positive rotation. A reverse flow region that developed behind the model is observed. The figure also shows vortical flow structures further downstream which resulted from the separation of the shear layers.

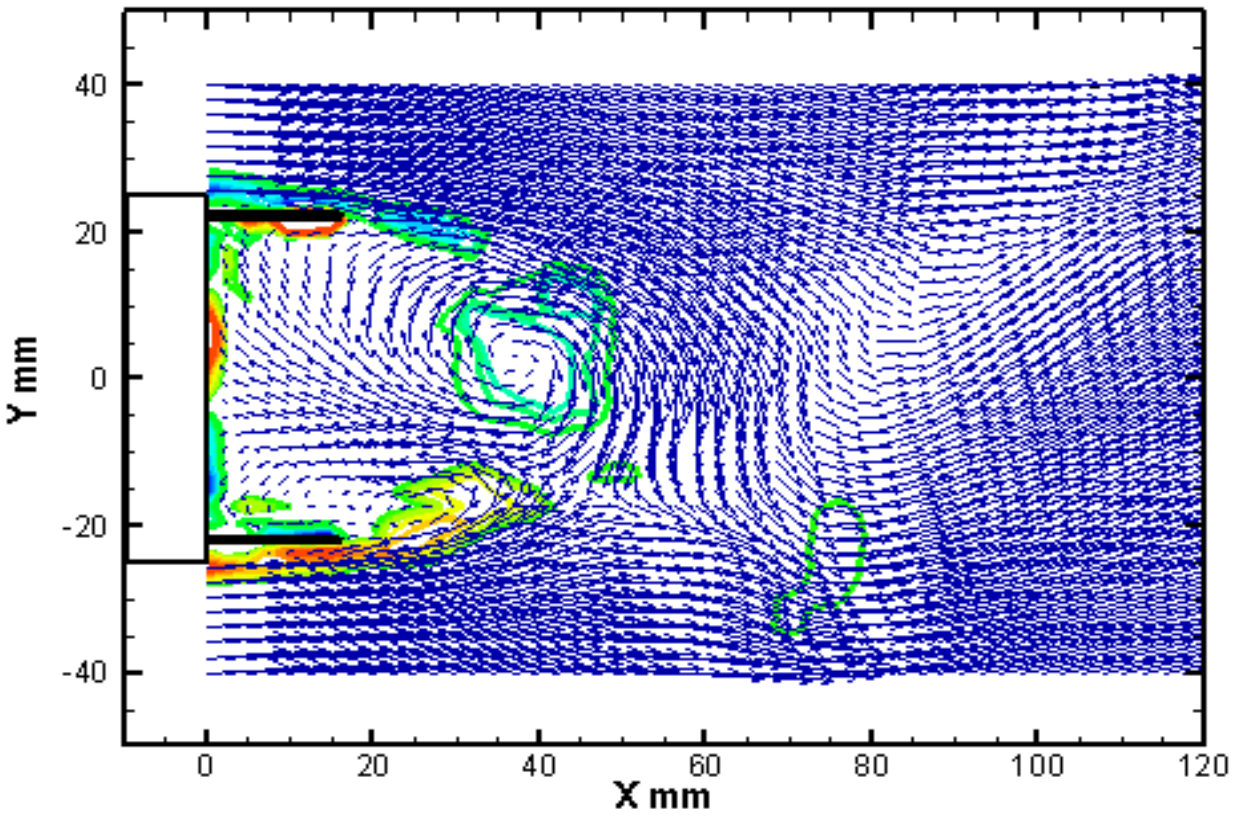

(a)

Figure 4.10 For caption see page 73.

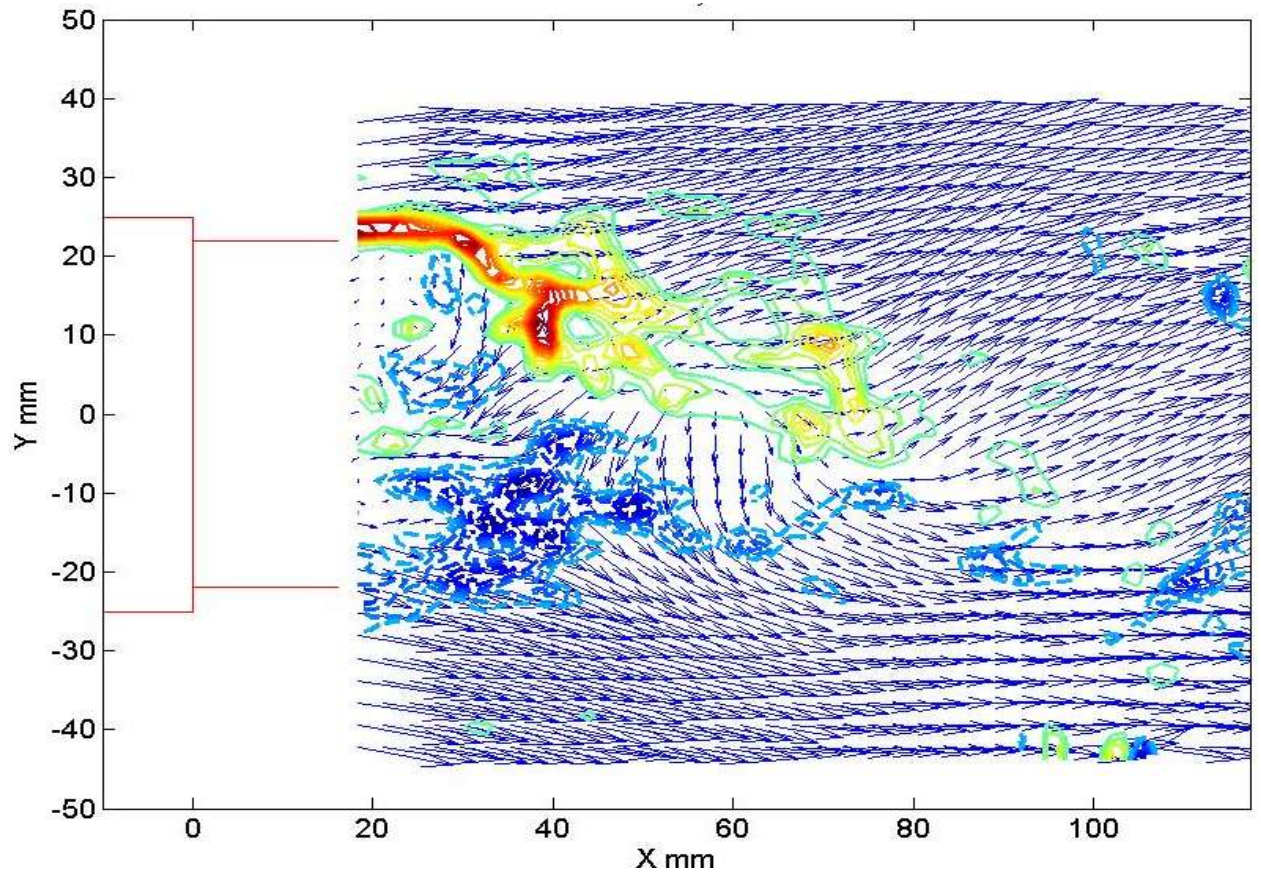

(b)

Figure 4.11 Instantaneous velocity and vorticity fields in the symmetry plane of the base model fitted with 1/3 h cavity: (a) LES, (b) experiment ([30])

A vector plot of the mean velocity field for the cavity model obtained with RANS, LES and experiment are shown in figure 4.12. As can be seen, the length of the separation region predicted by RANS is around 65 mm. On the other hand, this length is around 50 mm using LES. Comparing these values with experimental value, the difference is around 41.3% for RANS and 4.3% for LES. The figure shows clearly that the flow predicted by LES is in excellent agreement with experiment and that the RANS method fails to predict this flow.

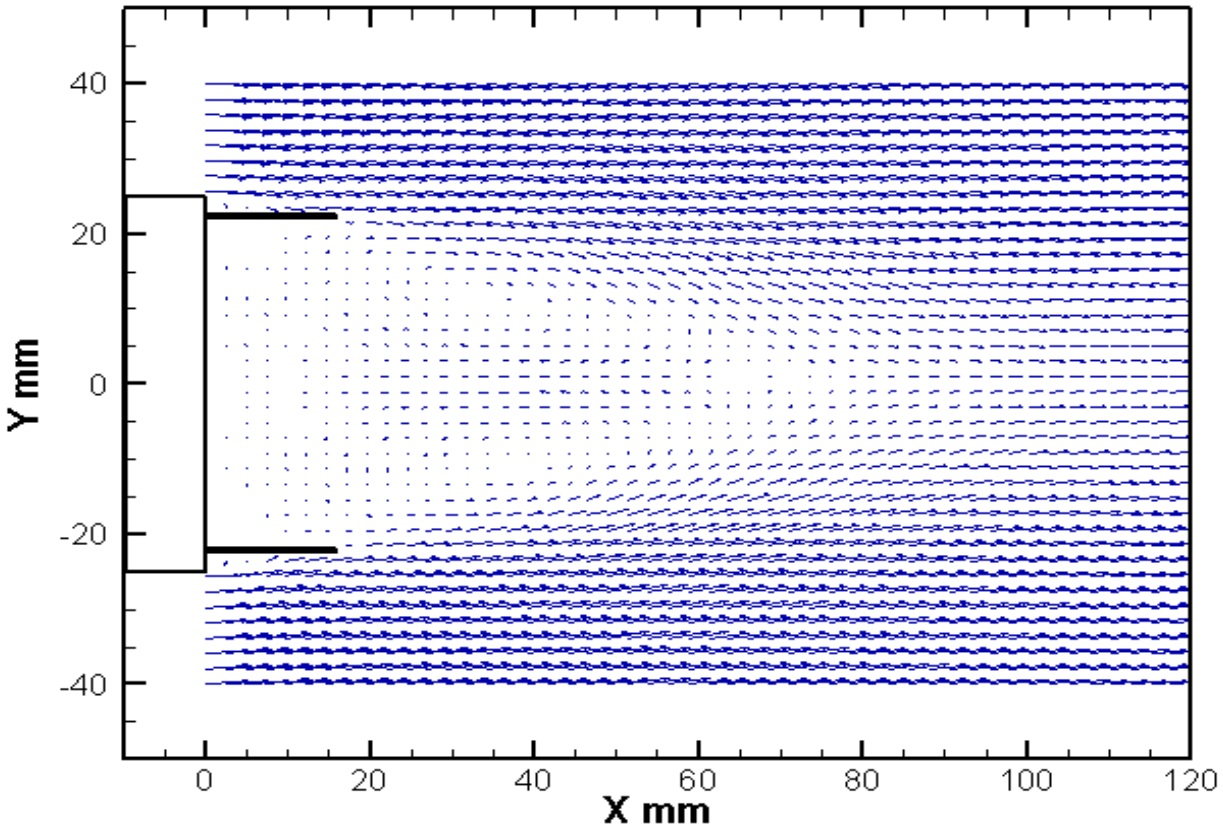

(a)

Figure 4.12 For caption see page 77.

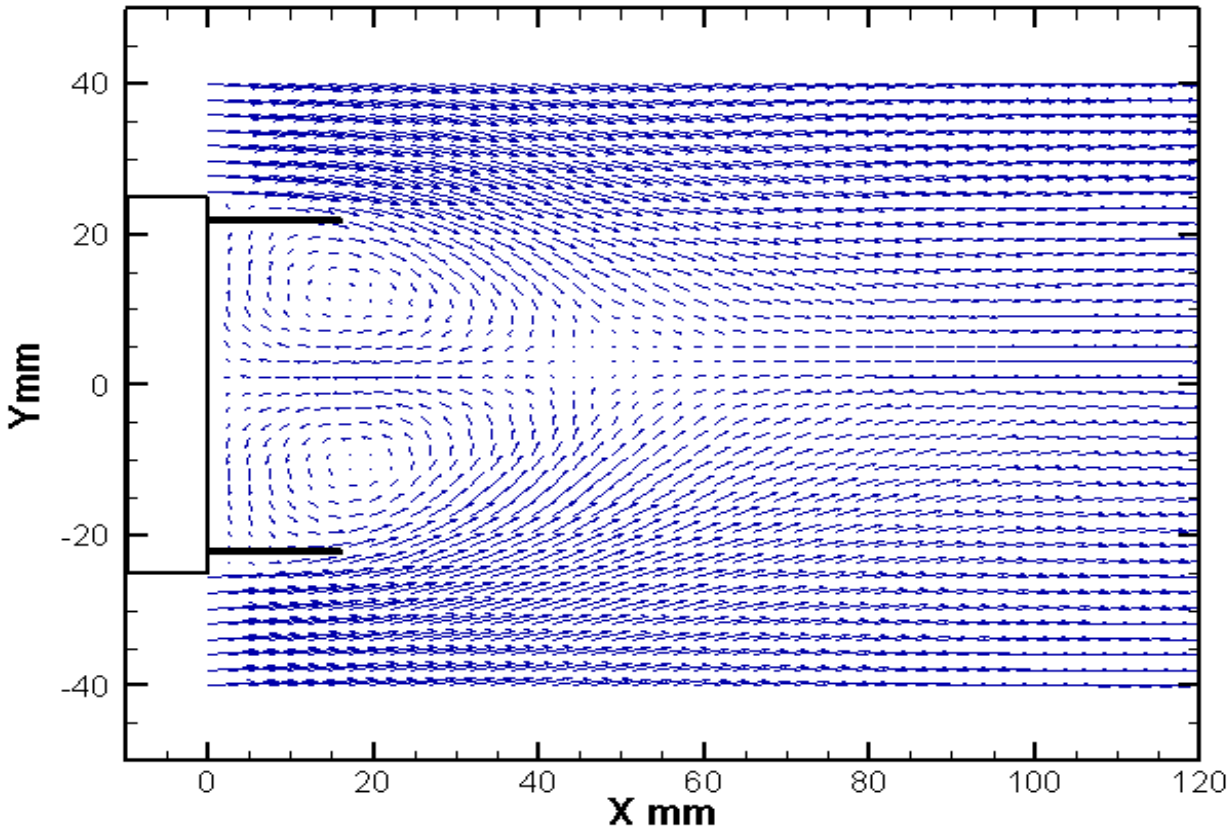

(b)

Figure 4.12 For caption see page 77.

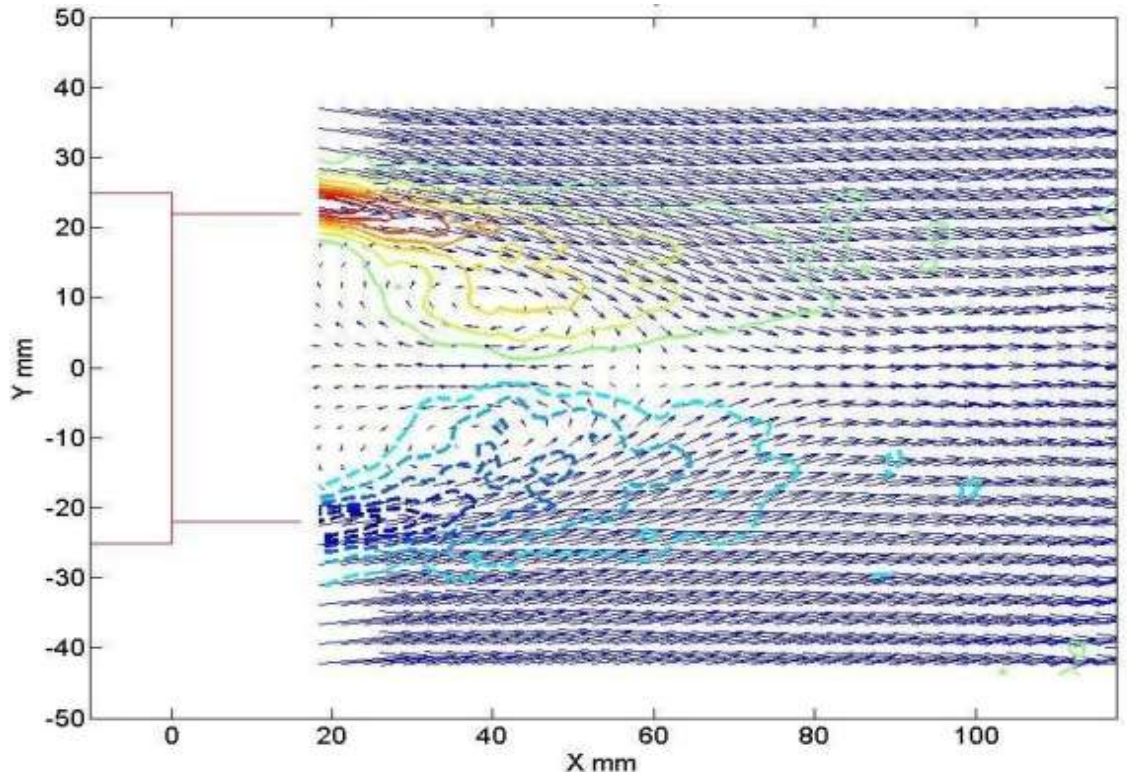

(c)

Figure 4.12 Mean velocity and vorticity fields in the symmetry plane of the base model fitted with 1/3 h cavity: (a) RANS, (b) LES and (c) experiment ([30]).

Figures 4.13 shows the mean flow streamlines in the near wake of the 1/3 h cavity at the symmetry plane using RANS, LES and experiment. Similar to the base model, there are two circulatory regions in which the flow rotates in direction opposite to each other. The recirculation regions formed are symmetric w.r.t to the center wake line. The length of the recirculation region is not changed much with the attachment of the 1/3 h cavity to the base model. Overall, LES simulation has good agreement with experimental results compared to RANS.

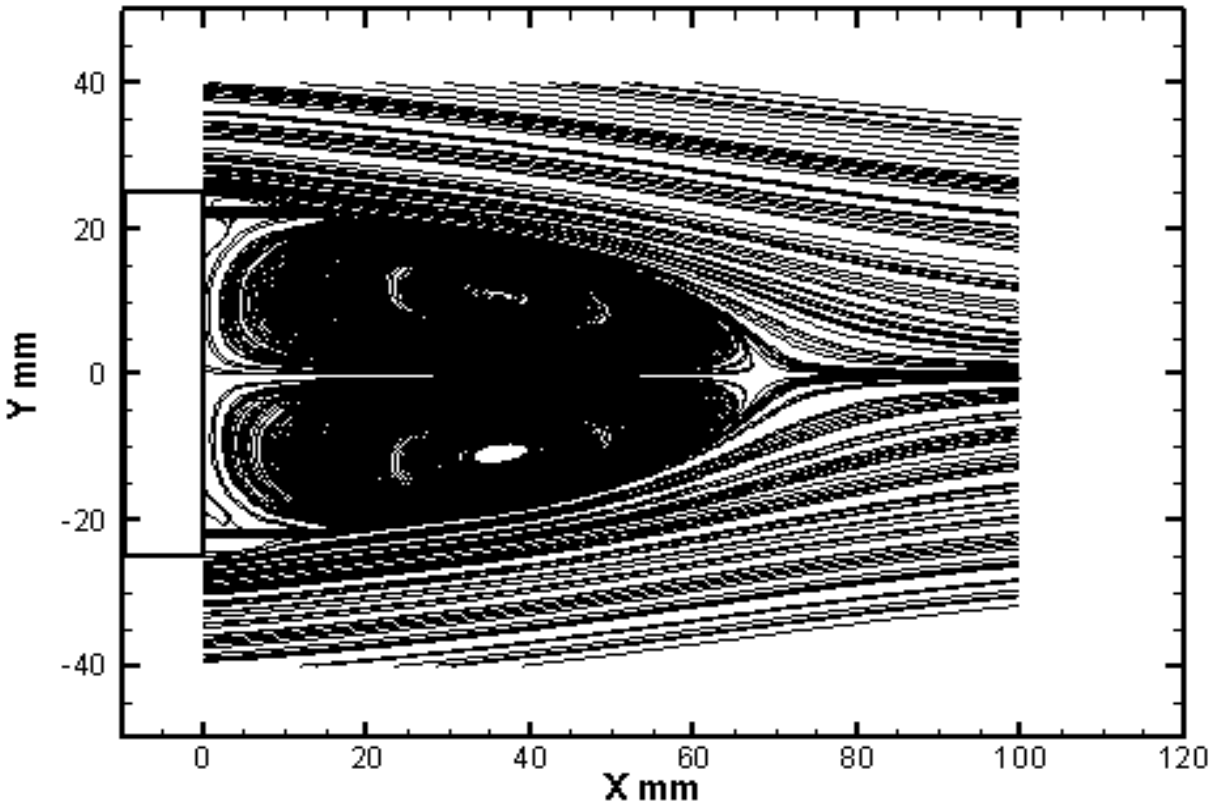

(a)

Figure 4.13 For caption see page 81.

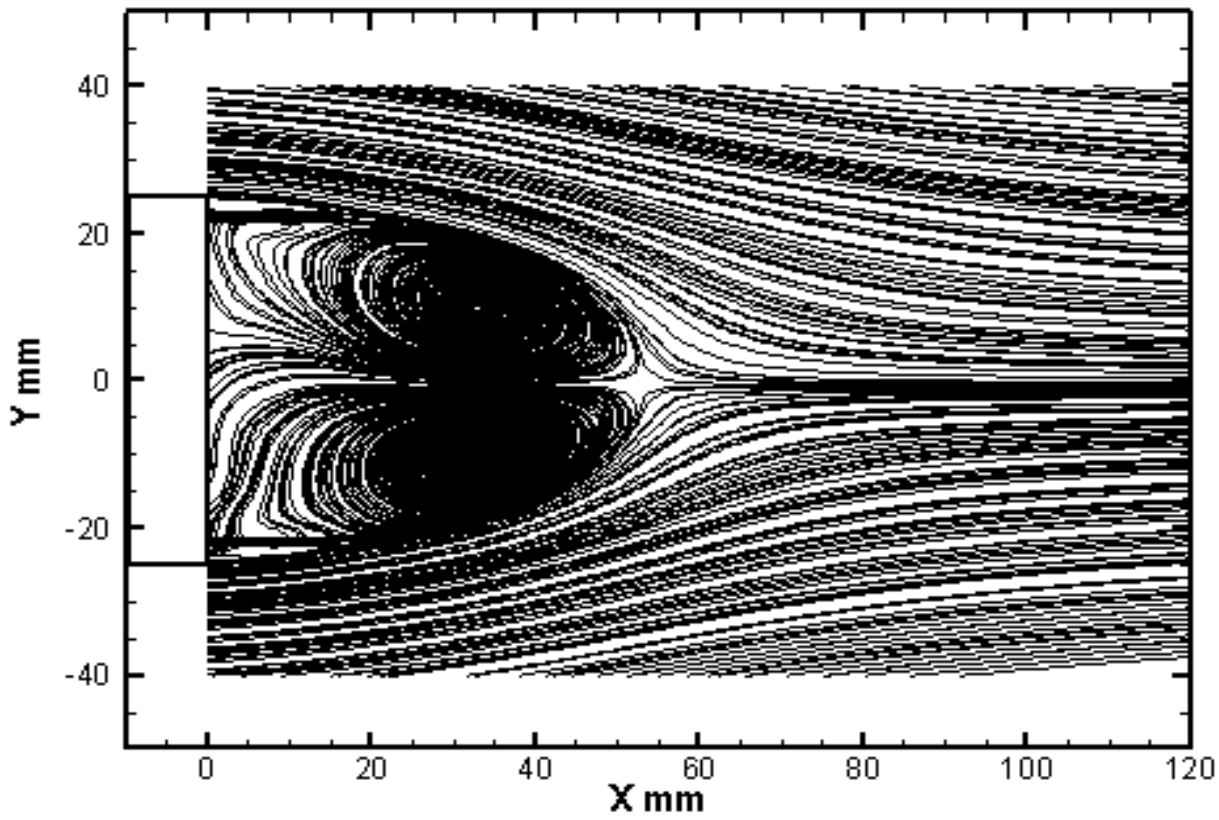

(b)

Figure 4.13 For caption see page 81.

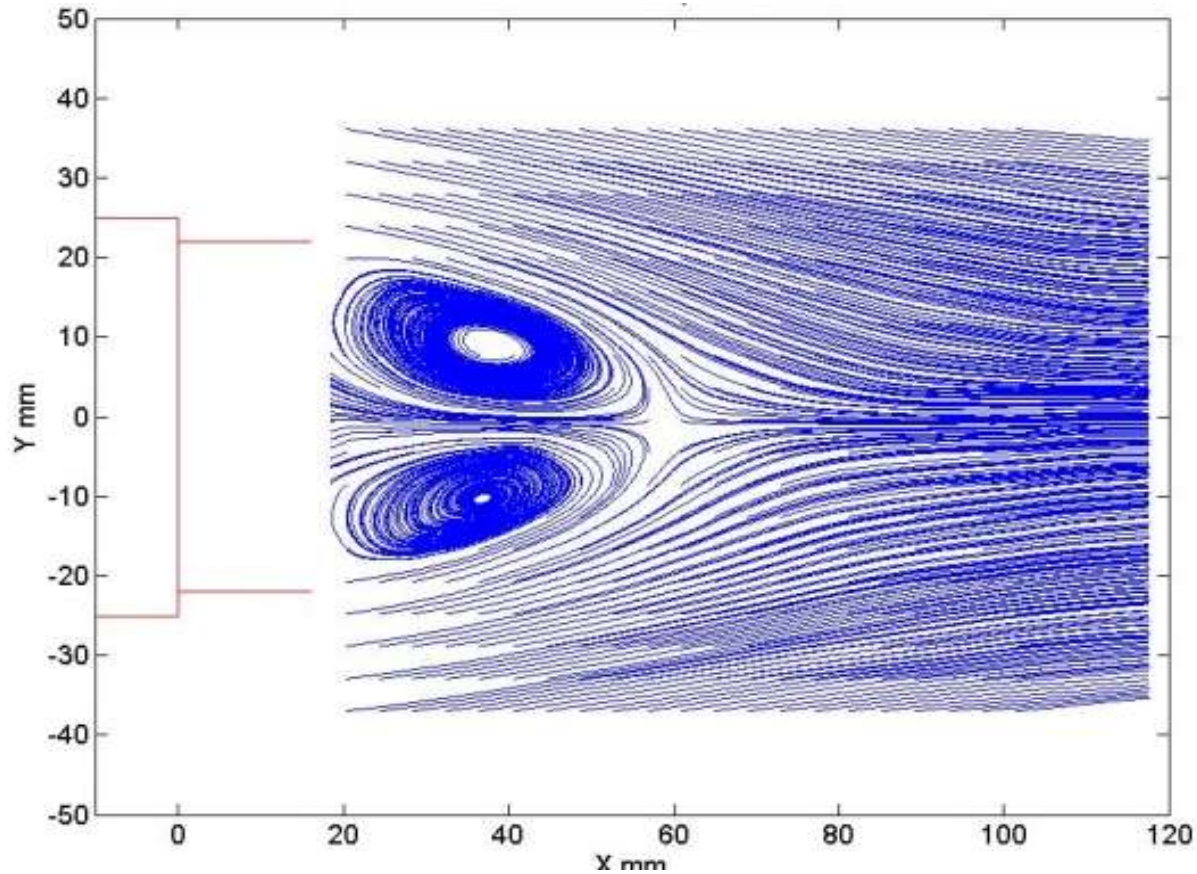

(c)

Figure 4.13 Streamlines of the mean velocity field in the symmetry plane of the base model fitted with 1/3 h cavity using: (a) RANS, (b) LES and (c) experiment ([30]).

4.5 Mean Velocity Profiles

4.5.1 Base Model

Figure 4.14 shows the mean streamwise and vertical velocity components in the symmetry plane of the near wake of the base model at four downstream locations of the base model, namely at x = 25, 50, 75, 100 mm. As shown in the figure RANS velocity profiles are nearly the same as experimental velocity profiles, however in the upstream locations LES are more accurate than RANS. Moreover, as can be seen also, the LES velocity profiles are in good agreement with experimental ones particularly at downstream locations. At x=25 mm it is shown that LES profiles is little different from experimental profiles while at x= 100 mm the LES and experimental profiles are exactly the. On the other hand, it is clear that LES prediction is more accurate than RANS particularly in the separated region.

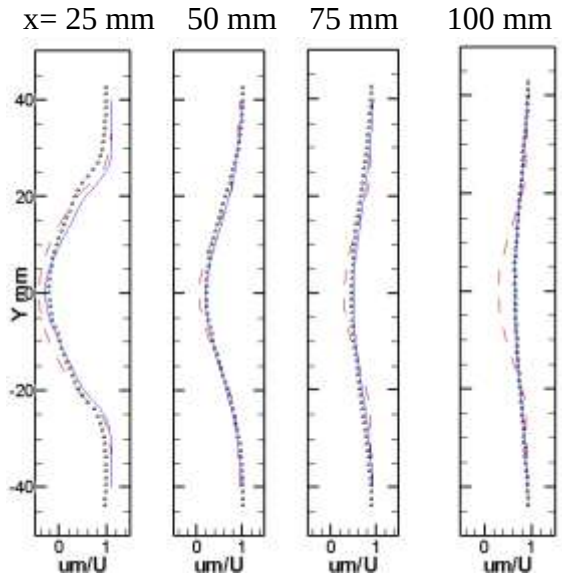

(a)

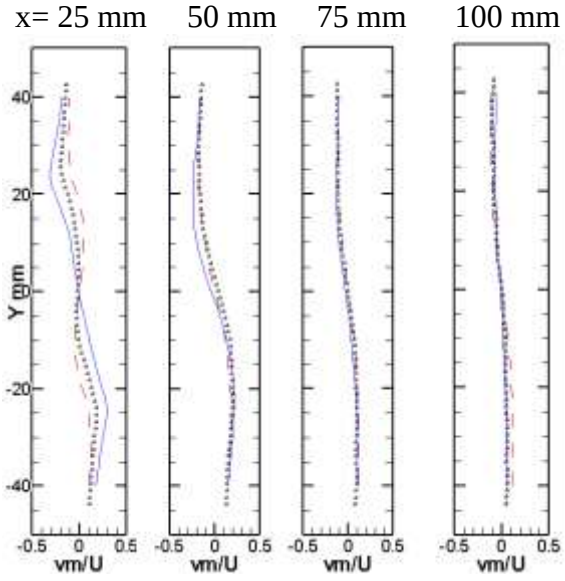

(b)

Figure 4.14 Mean velocity profiles in the symmetry plane of the wake of the base model: (a)u/U; (b) v/U.----RANS. –LES, ∆ experiment ([30]).

4.5.2 Base model fitted with 1/3 h cavity

Figure 4.15 shows the mean streamwise and vertical velocity components in the symmetry plane of the near wake of the base model fitted with 1/3 h cavity at four downstream locations x = 25, 50, 75 and 100 mm downstream the cavity. Figure 4.15 (a) and (b) show the streamwise and vertical mean velocity component respectively. This figure indicates that the flow is symmetric about the centre wake line at Y = 0. Note that the near wake is shifted by 16 mm (length of the cavity) when fitted with 1/3 h cavity. Comparing between LES and RANS results with experiment results, the LES profiles is little different at x=25 mm but at x= 100 mm they are exactly the same as experimental results. For the RANS profiles, however, difference is large when compared with experiment specially in the separated region. There is a reverse flow region between x ~18 mm and 58 mm. The curves in the plots are similar to that of figure 4.14 (a) and no major changes are seen in the curve pattern. As shown in the figures 4.15, The velocity profiles from LES generally agreed well with the experimental data near to the end of recirculation region.

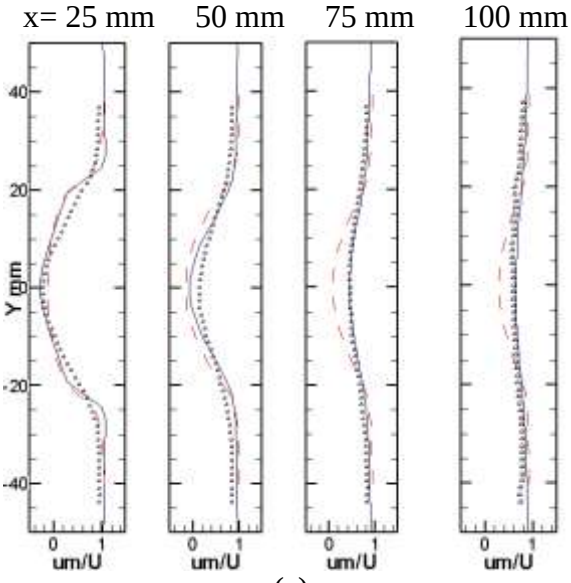

(a)

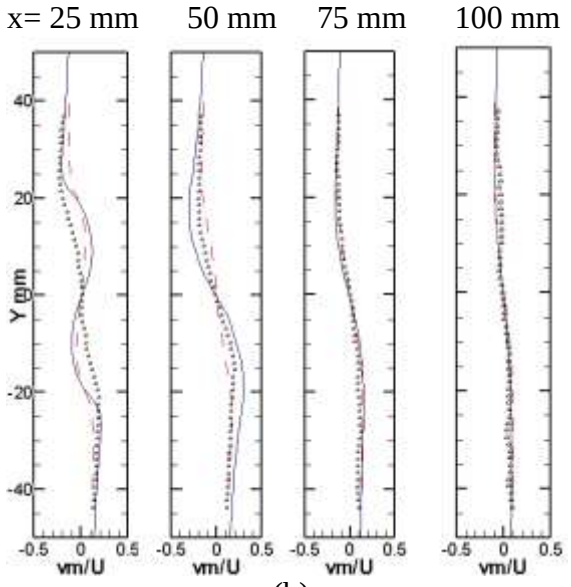

(b)

Figure 4.15 Mean velocity profiles in the symmetry plane of the wake of the base model fitted with 1/3 h cavity: (a) u/U; (b) v/U.---- RANS. –LES, ∆ experiment ([30]).

CHAPTER 5

CONCLUSION AND RECOMMENDATIONS

5.1 Conclusions

A numerical investigation of the flow around an elliptical bluff body using RANS and LES was conducted. The simulations were carried out at a Reynolds number of 2.6×10^4 based on the height of the body using Spalart-Allmaras RANS model while the LES were performed using Smagorinsky dynamic model. A grid-independence test was conducted using three grids which contain 0.85M, 1.3M and 1.7M cells, respectively. This test shows that the results are grid-independent. Since the LES computation require massive computer memory and power and due to the limitation of our computer resources, it was carried out on grid 2(1.3M cells). The LES results predicted the mean flow field in the near wake with good accuracy as compared to the experimental mean flow field obtained using. The base pressure results show that the base pressure coefficient for the base model was around -0.56, which agrees well with the experimental results .By attaching the cavity, the base pressure has increased. The increase in base pressure coefficient was around 44% using 1/3 h cavity and this agrees well with the experimental measurements. The drag force acting on the base model alone and with the attachment of the 1/3h cavity were obtained. The RANS predicted drag coefficient of 0.56 for the base model and 0.471 for the cavity model. This represent a difference of 8% for the base model and 34% for the cavity model when compared with experiment drag coefficients (0.61 for the base model and 0.35 for the cavity model). For the

LES, the drag coefficient of the base model was around 0.65 (6.5% difference) and using the cavity, the drag coefficient was reduced to around 0.37 (5.74% difference).

Details of the mean velocity components have been compared with experimental data at various locations in the wake region of the flow. The LES results show generally very good agreement with the experimental findings. Observation on the comparison between LES and RANS shows that LES predicted the mean flow field more accurately than RANS particularly downstream the recirculation regions. The length of the recirculation region was over predicted by RANS compared to LES. The prediction of this length by LES was in excellent agreement with experimental measurement.

5.2 Recommendation

The mesh (1.3×10^6 cells) used in LES computation is considered to be moderate at the Reynolds number tested (2.6×10^4). This was limited by our computer resources and lack of high performance computing center in the departments or university. Therefore, the following recommendations are proposed:

- The LES computation needs to be carried out on finer grid (twice or 3 times the number of cells in grid 2) in order to resolve most scales in the flow.

- More cavities of different shapes such as multi-stepped cavity, different length open cavities and angled cavities of other different angles can be tested for base drag and wake properties for the same two-dimensional bluff bodies.

- The successful CFD strategies shown above can be utilized to compute the flow around more complex geometries such as trucks, airplanes and cars to predict the flow around aerodynamics forces acting on these geometries.

- Computation of the flow around the model considered in this study can be performed using Detached Eddy Simulation (DES). DES is a promising tool that requies less computing resources without sacrificing the solution accuracy.

- More simulations at higher Reynolds numbers can be conducted for further understanding of the flow characteristics around such bodies, especially simulations at similar aspect ratio.

REFERENCES

[1] Launder, B. E. and Spalding J.L. "Mathematical models of turbulence", Academic Press, New York, 1972.

[2] Arpaci, V. S. and Larsen P. S. "Convective Heat Transfer, Prentice-Hall", Englewood Cliffs, NJ, 1974.

[3] Zdravkovich, M.M. "Review and classification of various aerodynamic and hydrodynamic means for suppressing vortex shedding", J. Wind Engineering and Industrial Aerodynamics, Vol. 7, 1981, pp. 145-1 89.

[4] Nash, J.F., "A Review of Research on Two-dimensional Base Flow", *Aerodynamics Division, N.P.L*, Reports and Memoranda No. 3323, March, 1962.

[5] Tanner, M., "Reduction of base drag, Program in aerospace sciences",Vol.16, 369-384, 1975.

[6] Viswanath, P. R. and Patil, S. R., "Drag characteristics of a class of non- axisymmetric after bodies at high speeds", *NALPD: EA 9407*, 1994.

[7] Maxworthy, T., "Experiments on the flow around a sphere at high Reynolds numbers", J. of Applied mechanics, 91, 1969, pp.369-607

[8] Quadflieg, H., "Verringerung des Kugelwiderstandes crberhalb der kritischen Reynolds-zahl bei stationaerer Grenrschichtsabloesung", Abhandlungen aus dem Aerodynamischen Institut der RVVTH, Heft 22. Sonderband, Aachen,1975, pp.49-51.

[9] Petrusma, M. S. and Gai, S. L., "The Effect of geometry on the base pressure recovery of the segmented blunt trailing edge", *Aeronautical Journal*, Vol. 98,1994, pp. 267.

[10] Tombazis, N. and Bearman, P.W., "A study of three-dimensional aspects of vortex shedding from a bluff body with a mild geometric disturbance", *Journal of Fluid Mechanics*, Vol. 330, 1997, pp. 85-112.

[11] Park, H., Kim, J., Hahn, S., Kim, J., Lee, D., Choi, J., Jeon, W. and Choi, H., "Drag reduction in flow over a two-dimensional bluff body with a blunt trailing edge using a new passive device", *Journal of Fluid Mechanics*, Vol.563,2006, pp.389-414.

[12] Kim, J., Hahn, S., Kim, J., Lee, D., Choi, J., Jeon, W. and Choi, H., "Active control of turbulent flow over a model vehicle for drag reduction", *Journal of Turbulence*, Vol.5:1, 2004, pp.112.

[13] Bearman, P. W., "The effect of base bleed on the flow behind a two- dimensional model with a blunt trailing edge", *Aeronautical Quarterly*,Vol.18,1967, pp. 207.

[14] Michael, J., Molezzi, J. and Craig, D., "Study of Subsonic Base Cavity Flow field Structure using Particle Image Velocimetry", *AIAA Journal*,Vol.33, No.2, November 1990, pp. 201-209.

[15] Bahram, K., Zhang, S., Koromilas, C., Balkanyi, S. R., Luis, P., Bernal, G., Iaccarino, P. Moin., "Experimental and Computational Study of Unsteady Wake Flow behind a Bluff Body with a Drag Reduction Device", *Society of Automotive Engineers*, Vol. 1, 2001, pp.207.

[16] Krajnovic, S. and Davidson, L.,"Large Eddy Simulation of the Flow around a Simplified Car Model", 2004, pp. 2004-01-0227.

[17] Hinterberger, G.,Villalba, M. and Rodi, W., “Large Eddy Simulation of flow around the Ahmed body”, In Lecture Notes in Applied and Computational Mechanics, 2004, Springer Verlag, ISBN: 3-540-22088-7.

[18] Sohankar, A., Norberg, C., Davidson L., “Simulation of three-dimensional flow around a square cylinder at moderate Reynolds numbers”, Phys. of Fluids, Vol.11, No.2,1999, pp. 288- 306.

[19] Okajima, A., “Flow around a rectangular cylinder with a section of various depth / breath ratios”, Journal of Wind Engineering, Vol.17, 1983, pp.79-80.

[20] Yu, D., Kareem A., “Parametric study of flow around rectangular prisms using LES”, Journal of Wind Engineering and Industrial Aerodynamics, Vol.77, 1998, pp. 653-662.

[21] Ferziger J., “Subgrid scale modeling”, Large Eddy Simulation of Complex Engineering and Geophysical Flows, Cambridge University, 1993, pp.37-54.

[22] Boussinesq, J., “Théorie de l'écoulement tourbillant (Theories of swirling flow)”,Mém. prés. Par div. savants à l'Acad. Sci. Paris, Vol.23, 1877.

[23] Blazek, J., Computational Fluid Dynamics: Principles and Applications, Elsevier Science Ltd, Oxford England, 2001.

[24] Davidson, L., “An introduction to turbulence models”, Department of Thermo and Fluid Dynamics, Chalmers University of Technology, Sweden, 2003.

[25] Tremblay, F., “Direct and large-eddy simulation of flow around a circular cylinder at subcritical Reynolds numbers”, Dissertation submitted for the degree of PhD, Technical university of Munich, 2001.

[26] Yuan, S., “Foundation of fluid mechanics”, Prentice Hall, New Jersey, 1987.

[27] Hoerner, S.F., Fluid dynamic drag, Horner fluid dynamic, New Jersey, 1958.

[28] Viswanath, P.R., "Flow Management Techniques for Base and After body Drag Reduction", *Program in Aerospace Sciences*, Vol. 32, 1996, pp.79-129.

[29] Nash, J., "A discussion of two-dimensional turbulent base flows", 1967, A.R.C.R&M.34 68.

[30] Abdurrahman, A., "Effect of base cavities on the drag and wake of a two-dimensional bluff body", Master Thesis, KFUPM, Aerospace Engineering Department ,2009.

[31] Issa, R. I., "Solution of the Implicitly Discretized Fluid Flow Equations by Operator-Splitting", *J. of Computational Physics*, 1985, pp.62:40-65.

VITA

- Khalid Qaied AL-Anazi
- Nationality; Saudi Arab
- Obtained Bachelor's degree in Aerospace Engineering from King Fahd University of Petroleum and Minerals, Dhahran Aug. 2004
- Researcher Assistance in KFUPM; 2004 – 2007
- Machinery Engineer in KEMYA (SABIC & ExxonMobil); 2007- present
- Completed Master's Degree requirements at King Fahd University of Petroleum & Minerals, Dhahran, Saudi Arabia in 2010.
- Address; Jubail Industrial City, Box #10084 Jubail Industrial City 31961, Kingdom of Saudi Arabia, E-mail: *gaied2006@hotmail.com*.